A length-scale insensitive cohesive phase-field interface model: application to concurrent bulk and interface fracture simulation in Lithium-ion battery materials

Wan-Xin Chen[a,*], Xiang-Long Peng[a], Jian-Ying Wu[b], Orkun Furat[c], Volker Schmidt[c], Bai-Xiang Xu[a,*]

[a]*Division Mechanics of Functional Materials, Institute of Materials Science, Technischen Universität Darmstadt, Darmstadt 64287, Germany*
[b]*State Key Laboratory of Subtropical Building and Urban Science, South China University of Technology, Guangzhou 510641, China*
[c]*Institute of Stochastics, Ulm University, 89069 Ulm, Germany*

Abstract

A new cohesive phase-field (CPF) interface fracture model is proposed in this paper. It employs an exponential function for the interpolation of fracture energy between the bulk phase and the interface, and its effective interface fracture energy is solved based on the Euler-Lagrange equation of the phase-field theory and the consistency to the cohesive zone model (CZM) in the sharp interface concept. Comparison to other interface models in the literature clearly shows that the above energy consistency is essential to ensure the insensitivity of the results to the length-scale parameters for regularization of the crack surface and of the interface. The proposed interface model can be conveniently implemented via the relaxation solution of an Allen-Cahn equation, which offers high flexibility in handling structures of complicated interface topology. The proposed CPF interface model is employed further to derive a thermodynamically consistent chemo-mechanical model relevant to Lithium-ion battery materials. Finite-element simulations confirm the model's ability to recapture the competition between bulk and interface fractures, while also demonstrate its merits of length-scale insensitivity and consistency with CZM results. The model is eventually applied in polycrystalline electrode particles, which are reconstructed from images with segmented interfaces, confirming the expected computational advantages and the length-scale insensitivity in multi-physical context.

Keywords: Cohesive phase-field fracture; Cohesive zone model; Interface fracture energy check; Length-scale insensitivity; Chemo-mechanical fracture; Concurrent bulk and interface fracture

1. Introduction

Advanced material systems are inherently heterogeneous, often comprising multiple phases or distinct bulk-interface regions in their complex microstructures. Examples of such materials include engineering materials like fiber-reinforced cement composites [1], coating systems [2], multiphase composites [3], and composite laminates [4], as well as biomaterials like bones [5] and energy materials like Lithium-ion batteries (LIBs)[6]. A common phenomenon in these materials is the concurrent occurrence of bulk and interface fracture, which degrades the overall

*Corresponding author(s).
Email addresses: wanxin.chen@tu-darmstadt.de (Wan-Xin Chen), xu@mfm.tu-darmstadt.de (Bai-Xiang Xu)

capacity and performance of the materials and structures [7]. This necessitates the development of computational models to accurately recapture and predict these fracture behaviors, thereby enhancing the reliability and durability of these advanced materials.

To model the cracking behaviors at interfaces, the cohesive zone model (CZM) [8, 9] is widely used due to its ease of implementation for interfacial properties and its accuracy in reproducing experimental results. In the CZM, the discontinuous displacement jump at the interface is explicitly represented with cohesive interface element [10], and a constitutive relation between the (local) traction vector $\tilde{\boldsymbol{t}}$ and the (local) displacement jump vector $[\![\tilde{\boldsymbol{u}}]\!]$ is formulated, which is known as the traction-separation law (TSL). However, this approach exhibits challenges in modeling arbitrary cracks propagation within the bulk phase [10]. In the last two decades, the phase-field fracture model originally proposed by [11, 12], which utilizes a damage-like scalar variable to regularize the sharp crack and minimizes the total system energy within a variational framework, has been a popular candidate in modeling complex evolution of arbitrary cracks in the solids. In particular, [13, 14] proposed a cohesive phase-field (CPF) fracture model utilizing the parameterized energy degradation function and crack geometry function, which can reproduce the general softening laws of the CZM and ensure the results are insensitive to the choice of internal phase-field length-scale parameter b. Despite its extensive applications in modeling fracture problems in homogeneous materials, the phase-field model's ability to accurately simulate arbitrary cracks propagation in heterogeneous systems, which include both bulk phases and interfaces, remains limited.

The cohesive zone model for interface fractures and the phase-field model for bulk phase cracks, which represent discrete and smeared crack configurations respectively, are technically two distinct approaches, and integrating them into a unified framework is challenging, see [15–17]. However, bulk and interface fractures can happen simultaneously in heterogeneous systems, which are regulated by the energy-based material physics. In this context, we anticipate to utilize an unified material model in this manuscript, which can recapture both types of fracture at the same time. As reviewed following in Section 1.1, the phase-field fracture model is promising to be extended to recapture the interface fracture, while it still remains challenging and awaits for further improvements regarding the energy equivalency between the phase-field framework and the CZM, as well as the length-scale sensitivity issue of phase-field model, which will be the main focus of this paper. Moreover, the concurrent bulk and interface fracture in engineering materials happen mostly under multi-physical circumstance, as can be seen in Section 1.2, an important prototyping example is chemo-mechanical inter- and trans-granular fractures in Lithium-ion battery cathode materials. Extending the unified model to address chemo-mechanically coupled bulk and interface fracture and verifying its robustness in a multi-field context are also challenging points to be investigated in this paper.

1.1. Phase-field modeling of interface fracture

In order to model and simulate crack propagation in a heterogeneous system including bulk phase and interface, several attempts in recent years have been made to develop the phase-field model, trying to take into account the influence of interface on the fracture evolution process. One approach integrates the phase-field method for bulk

fracture with the cohesive zone model for interface crack, wherein the displacement jump across the interface is represented using either cohesive interface element [15–17] or a regularized form based on the phase-field approximation [18]. This approach presents challenges in defining the coupling relations between the phase-field and cohesive zone damage, and it is cumbersome to numerically implement two types of material constitutive laws. The other popular approach is to represent the interface in a diffused manner within the phase-field framework, namely, the fracture energy in the domain is interpolated between that of the bulk phase and the interface [19–21], which can be conveniently implemented based on an auxiliary indicator solved from the Allen-Cahn equation [18]. This diffusive approach provides significant flexibility in modeling crack propagation at interfaces, which has inspired extensive applications [22, 23], including Lithium-ion batteries [24–26] in the multi-physical context. However, as will be shown later in this paper, the aforementioned diffusive treatment on the interface fails to ensure the (integrated) fracture energy within the phase-field framework consistent with that defined in the cohesive zone model, which correspondingly leads to the length-scale sensitivity [14], i.e., parameters regularizing the crack surface b and interface L have essential impacts on fracture and mechanical behaviors of structures.

To address the aforementioned length-scale sensitivity issue, [27, 28] first proposed to use the effective interface fracture energy w.r.t the choices of length-scale parameters (b and L) in the phase-field interface model. This approach, which is referred to as Model-S1 in Section 3.1, tries to constrain the (integrated) fracture energy dissipation to be equivalent to that defined in the cohesive zone model for a sharp interface. Nevertheless, these studies have found that interface fracture resistance is always underestimated in the simulations, which is attributed to the use of the phase-field profile of a homogeneous bulk phase when solving the energy consistency constraint equation. On the basis of that, [29, 30] introduced the Euler-Lagrange equation to analytically express the phase-field profile in a heterogeneous domain with both bulk and diffusive interface (see Model-S2 in Section 3.1). They successfully determined the proper effective fracture energy to achieve interface fracture energy consistency and interface-width insensitivity. It's worth noting that, above derivations of the effective interface fracture energy are all applicable to the stair-wise interpolation of materials properties between the bulk phase and the interface, thanks to the phase-field profile being analytically solvable from the Euler-Lagrange equation. However, as proved by extensive applications under purely mechanical [19–21] and multi-physical contexts like Lithium-ion batteries [24–26, 31], the exponential interpolation of material property implemented with an auxiliary Allen-Cahn indicator offers greater flexibility compared to the stair-wise one in handling structures containing complex interface topology, particularly for the image-based reconstructed 3D polycrystalline microstructure [31]; nevertheless, such length-scale insensitive phase-field interface model still remains absent in the literature.

1.2. Chemo-mechanical inter- and trans-granular fractures in LIB cathode materials

Lithium-ion batteries have emerged as a revolutionary technology, powering a diverse range of essential devices from smartphones to electric vehicles, and serving as one of the promising candidates for next-generation energy storage technology [32, 33]. Despite their promising merits and widespread commercial deployment, LIBs suffer from

significant performance and capacity fading in the cycles of charging and discharging, in particular, damage and fracture induced chemo-mechanical degradation [34] has been recognized as one of the key mechanisms influencing their longevity and reliability. Extensive experimental research is underway to elucidate the intensive existence of cracks and their critical role in causing deterioration in battery systems, e.g., lithium dendrite formation [35] induced crack propagation in the electrolyte, fracture in the silicon anode particle due to significant volume change[36], fracture of cathode particles [37], failure of solid electrolyte [38], interfacial delamination [39], and so on. Those fractures within the LIBs impact the electrochemically active surface area, hinder charge-transfer reactions at the electrode/electrolyte interfaces, and eventually lead to increased cell resistance and reduced available capacity [7, 39].

In this paper, we will focus on the damage and fracture behaviors of cathode particles in the LIBs. Most commonly available cathodes, such as $LiCoO_2$, $LiMn_2O_4$ and $LiNi_xMn_yCo_{1-x-y}O_2$ (NMC) and so on, exhibit a polycrystalline microstructure [40] in nature, those secondary particles (order 10-20 μm) are comprised of randomly oriented single grains, also referred to as primary particles [41]. The interfaces where crystalline grains meet are termed as grain boundaries (GBs). During (dis)charging cycle, Li (de)intercalation can induce anisotropic volume change (expansion/shrinkage) [42], which can generate inhomogeneous stress distribution in the structures. Typically, GBs with lower mechanical failure resistances [7, 43] act as potentially starting points with damage nucleation and crack propagation, forming inter-granular (interface) fracture at the GBs [7, 44]; in addition, with introduced defects (e.g., vacancy and surface curvature) and the random grains' orientations [45], trans-granular (bulk) cracks within the primary particles can also be observed in the experiments [46, 47]. Furthermore, in a multi-physically coupled context, cracks damage the pathways within the electrode structure for lithium transport, leading to degradation in the chemical diffusion process [48], potential grain isolation [31], and overall deterioration of cathode capacity [6].

The aforementioned evidences and insights garnered from experiments provide a valuable opportunity for conducting numerical investigations into the chemo-mechanical behaviors of polycrystalline cathode particles. Several computational endeavors have been undertaken to model the chemo-mechanical behaviors in typical LIBs electrode, e.g., lithium (de)intercalation induced mechanical stresses [49–51], phase segregation captured with a Cahn-Hilliard phase-field model [51, 52], electrochemical performance and embrittlement degradation over (dis)charging cycles (fatigue) [53–55], influences of mechanical and transport features of grain boundaries [56–58], etc. See [34, 59, 60] for comprehensive reviews on chemo-mechanical modeling of LIBs.

With a particular focus on damage and fracture behaviors in the LIBs cathode materials in this paper, here available chemo-mechanically coupled models are reviewed. Inspired by its widespread use in purely mechanical context, the cohesive zone model [10] has been successfully extended to chemo-mechanical scenario and is likely the most popular candidate among other available options, see [53, 55, 56, 58, 61–64] for numerous applications in LIBs. The CZM excels in recapturing cracks propagation along the GBs and the corresponding across-GBs degradation in electrode particles. However, its ability to predict arbitrary trans-granular cracks within the grains is limited. Comparatively, phase-field fracture model originally proposed by [12, 65], which demonstrates advantages in simulating complex evolution of arbitrary cracks, showcases robust capabilities in modeling chemo-mechanical fracture and the induced

degradation in the LIBs, see considerable successes in [48, 54, 66–73]. Despite the noteworthy contributions, those phase-field models for LIBs operate at the macro-scale level and overlook the intricate polycrystalline microstructure comprised of diverse grains and complex GBs, where the latter typically exhibits weaker fracture properties [7, 43]. Consequently, diverse fracture modes including inter- and trans-granular cracks [44, 46, 47] observed in the experiments can not be recaptured in aforementioned simulations.

To account for the heterogeneity within the cathode particle microstructure and predict both inter- and trans-granular failure modes, several endeavors have been made to incorporate interface fracture property into the phase-field framework, e.g. the sharp interface fracture energy is interpolated with that of the bulk phase in the domain, through either a stair-wise function [31, 74] (refer to Model-S0, see Section 3.1) or an exponential function [24–26] (refer to Model-E0, see Section 3.1) based on the predefined auxiliary indicator solved from the Allen-Cahn equation [18]. Such approach can qualitatively simulate (and distinguish) diverse cracking modes at the GBs/interfaces or within the grains/bulks, whereas it will be shown later in this paper, it can not ensure the evaluated interface fracture energy (i.e., the amount of energy consumed for unit crack surface) within the phase-field framework to be consistent with that of a sharp interface defined in the cohesive zone model [10]. Furthermore, the fracture energy dissipation for interface crack strongly depends on the choices of two length-scale parameters b and L, which are for respectively regularizing the crack surface and interface, so that length-scale sensitive outcomes would be anticipated, e.g., different fracture patterns and quantitative structural responses (e.g., reaction force) are obtained with varying b or L in the simulations. □

In this paper, our primary goal is to develop a new length-scale insensitive cohesive phase-field interface fracture model and apply to the chemo-mechanical simulations of polyscrystalline structures with complicated GBs topology within the LIB materials. We utilized an exponential interpolation of fracture energy between bulk phase and interface on the basis of the solution of an Allen-Cahn equation. The effective interface fracture energy is introduced and derived based on the Euler-Lagrange equation of the phase-field theory, so that the integrated phase-field fracture energy can be ensured to be equivalent to the sharp value defined in the cohesive zone model. With multi-dimensional and multi-physical extensions in a thermodynamically consistent manner, the model can simulate the chemo-mechanical inter-/trans- granular fractures in the Lithium-ion battery materials, particularly with following merits expected, e.g., consistency with predictions from the CZM, length-scale insensitivity and flexibility dealing with complicated GBs topology.

2. Recap of phase-field bulk fracture model

In this section, the fracture energy dissipation due to bulk crack propagation within the phase-field framework is briefly recalled. Consider an 1D infinite long domain in Figure 1 (a) with $x \in [-\infty, +\infty]$ indicating the spatial coordinate. In the phase-field context, crack evolution is characterized by the phase-field variable $d(x) \in [0, 1]$ describing the material damage level, with $d = 0$ and $d = 1$ denoting sound and fully damaged material, respectively.

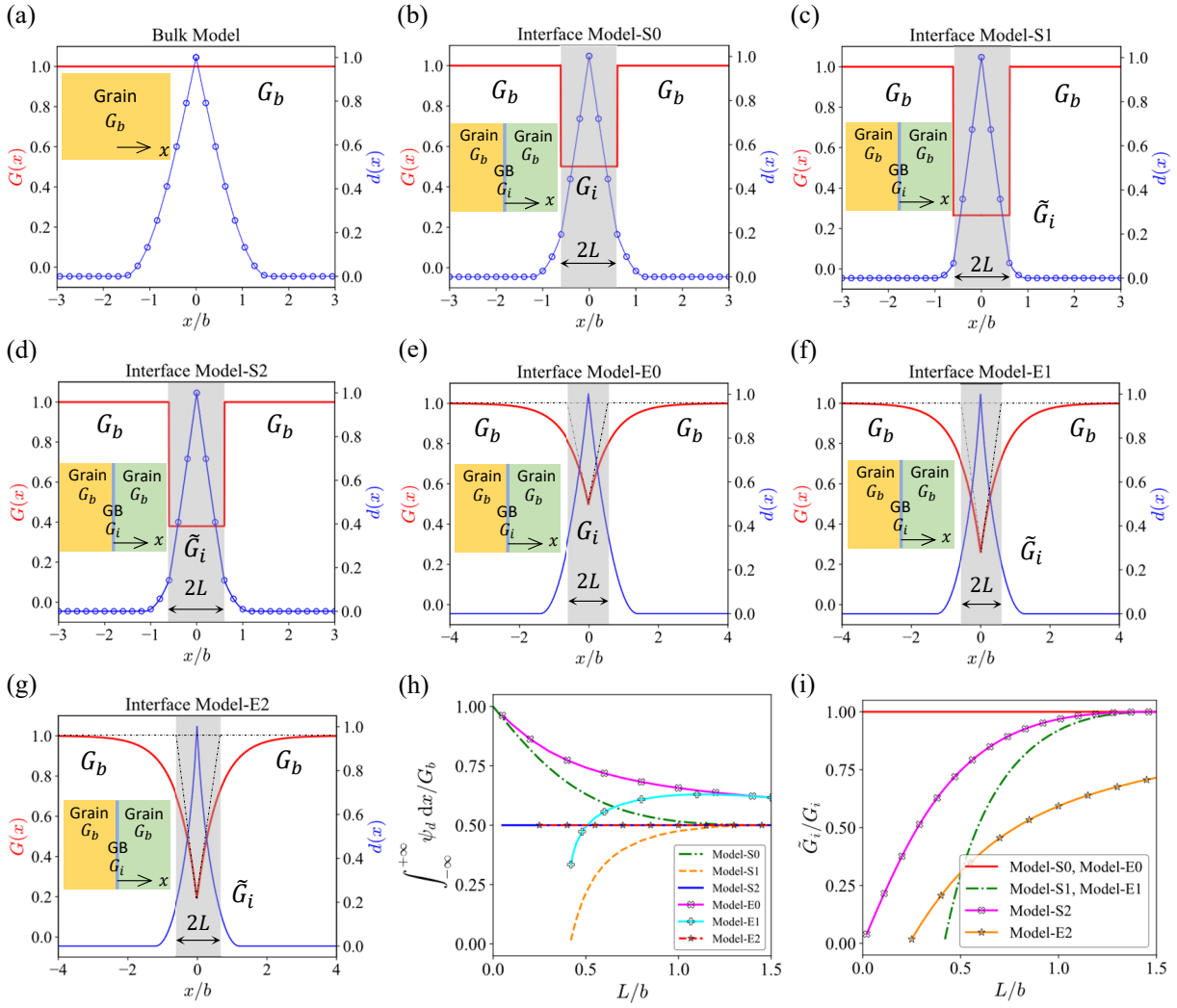

Figure 1: Figure (a) - (g) depict the spatial distributions of fracture energy $G(x)$ and the corresponding phase-field profiles $d(x)$ in the domain in diverse models. Figure (a) illustrates the case with uniform fracture energy in the bulk. Figure (b)-(e) depicts the domain composed of two grains (bulks) and an in-between diffusively represented GB (interface). For aforementioned sub-figures, red line indicates $G(x)$ normalized with bulk fracture energy G_b, blue line means $d(x)$ with markers showing its analytical solutions; we set $G_i = 0.5G_b$ and $L = 0.6b$ when demonstrating diverse interface models. Figure (h) shows the integrated phase-field fracture energy w.r.t. L/b in diverse interface models. Figure (i) illustrates obtained effective interface fracture energy $\tilde{G}_i$ normalized with G_i, w.r.t. L/b in diverse interface models. $G_i = 0.5G_b$ is assumed in Figure (h) and (i).

Follow the paradigm established by [12, 13], the bulk crack surface energy density functional ψ_d^b in 1D case in terms of the crack phase-field d and its spatial gradient d' is expressed as

$$\psi_d^b(d, d') = G_b\ \gamma(d, d'), \quad \text{with} \quad \gamma(d, d') = \frac{1}{\pi}\left(\frac{2d - d^2}{b} + bd'^2\right), \tag{2.1}$$

where G_b represents the critical energy-release rate or is called fracture energy of the bulk material, b is an internal phase-field length-scale parameter regularizing the crack, $2d - d^2$ as the local term expresses the crack geometry function in the cohesive phase-field fracture model [13].

The fracture energy dissipation of a bulk crack within the phase-field context can be obtained by integrating the density functional Eq. (2.1) over the domain, i.e.,

$$I(d) = \int_{-\infty}^{+\infty} \psi_d^b(d, d')\ \mathrm{d}x, \tag{2.2}$$

where the (equilibrium) phase-field profile $d(x)$ can be determined by minimizing Eq. (2.2), i.e.,

$$d(x) = \mathrm{Arg}\left(\inf I(d)\right), \tag{2.3}$$

leading to following Euler-Lagrange equation associated with the variational problem. Under irreversible evolution constraint [11] and proper boundary conditions (assuming the crack to occur in the middle $x = 0$),

$$\frac{\partial \psi_d^b}{\partial d} - \frac{\mathrm{d}}{\mathrm{d}x}\left(\frac{\partial \psi_d^b}{\partial d'}\right) = 0, \quad \text{subjected to } \ \dot{d} \geq 0,\ d(x = 0) = 1 \text{ and } d(x = \pm\infty) = 0, \tag{2.4}$$

phase-field optimal profile reads [13]:

$$d(x) = \begin{cases} 1 - \sin\left(\dfrac{|x|}{b}\right), & \text{when } |x| \leq \pi b/2 \\ 0, & \text{else} \end{cases}. \tag{2.5}$$

Accepting the aforementioned spatial distribution of phase-field variable at equilibrium state, it becomes evident that integrating the crack surface energy density functional — implemented through substituting Eq. (2.5) into Eq. (2.2), yields the value G_b.

$$\int_{-\infty}^{+\infty} \psi_d^b(d, d')\ \mathrm{d}x = \int_{-\infty}^{+\infty} \frac{G_b}{\pi}\left(\frac{2d(x) - d^2(x)}{b} + bd'^2(x)\right)\ \mathrm{d}x = G_b. \tag{2.6}$$

This value accurately quantifies the amount of energy required to create a sharp crack surface of unit area in the bulk material, which effectively remains consistency to the fracture energy defined in the classical cohesive zone model.

3. Length-scale insensitive cohesive phase-field interface model

In this section, we propose a new phase-field interface model, which can remain the consistency of interface fracture energy with that of the cohesive zone model, irrespective of the choice of different length-scale parameters. In particular, the merit of length-scale insensitivity is highlighted with comparison to several existing models from the literature. Eventually, the extension from 1D to multi-dimensional problems with numerical implementation details are presented.

3.1. Brief review on various phase-field interface models

In this subsection, several existing phase-field interface models from the literature are briefly reviewed, on the basis of the 1D problem setup. Our comparison focuses particularly on examining the consistency of interface fracture energy obtained from respective phase-field models with that of the cohesive zone model, as well as demonstrating the sensitivity or insensitivity of the models to length-scale parameters.

Similar to the bulk fracture case, in Figure 1, 1D infinite long domain is considered with an interface introduced in the middle where the crack is assumed to occur. Sharp interface is diffusively represented in the phase-field context, namely, material properties is interpolated between the bulk phase and the interface, e.g., with a particular focus on the fracture behavior, spatially varying fracture energy $G(x)$ in the domain is formulated in a general form,

$$G(x) = A(x)\tilde{G}_i + [1 - A(x)]\, G_b. \tag{3.1}$$

Here $A(x)$ is the general interpolation function in terms of spatial coordinate, $\tilde{G}_i$ denotes the effective interface fracture energy, which is interpolated with the bulk fracture energy G_b in the domain. With the introduced $G(x)$, the crack surface energy density functional ψ_d for interface fracture can be constructed,

$$\psi_d(x, d, d') = G(x)\, \gamma(d, d'), \quad \text{with} \quad \gamma(d, d') = \frac{1}{\pi}\left(\frac{2d - d^2}{b} + b d'^2\right). \tag{3.2}$$

Five existing phase-field interface models from the literature are compared in Table 1, and they are named as Model-S0 [31, 74, 75], Model-S1 [27, 28], Model-S2 [29, 76], Model-E0 [18, 20] and Model-E1 [21, 22], respectively. One category of models include Model-S0, Model-S1, Model-S2 in the paper, they adopt the Heaviside step function to achieve the interpolation, i.e,

$$A(x) = H(L - |x|), \qquad \text{with} \quad H(x) = \begin{cases} 1, & \text{for } x \geq 0 \\ 0, & \text{for } x < 0 \end{cases}, \tag{3.3}$$

thereby allowing its characterization as a heterogeneous material system featuring two phases: a bulk component with fracture property G_b and a diffusive interface with $\tilde{G}_i$ spanning a width of $2L$. Regarding the effective interface fracture energy $\tilde{G}_i$, Model-S0, Model-S1 and Model-S2 utilize different approaches to determine its specific value, with expressions listed in Table 1 and visualized in Figure 1 (i) for the respective models, details can refer to Appendix A. Under the constructed spatial distribution of fracture energy, the (equilibrium) phase-field profile $d(x)$ can be obtained by minimizing following integration,

$$d(x) = \mathrm{Arg}\,(\inf I(d)), \quad \text{with} \quad I(d) = \int_{-\infty}^{+\infty} \psi_d(x, d, d')\, \mathrm{d}x, \tag{3.4}$$

leading to the Euler-Lagrange equation of the variational problem,

$$\frac{\partial \psi_d}{\partial d} - \frac{\mathrm{d}}{\mathrm{d}x}\left(\frac{\partial \psi_d}{\partial d'}\right) = 0, \quad \text{subjected to } \dot{d} \geq 0,\ d(x = 0) = 1 \text{ and } d(x = \pm\infty) = 0, \tag{3.5}$$

with additional irreversible evolution constraint and proper boundary conditions listed above. By substituting obtained profile results $d(x)$ (see Figure 1 (b)-(d) for the respective models) into crack surface energy density functional Eq. (3.2) for integration in the 1D domain, we can obtain following phase-field interface fracture energy:

$$\int_{-\infty}^{+\infty} \psi_d(x, d, d')\, \mathrm{d}x = \frac{2}{\pi}\left[\left(\frac{\pi}{2} - \tan^{-1}\left[\frac{G_b}{G_i}\tan\left(\frac{L}{b}\right)\right] + \frac{L}{b}\right)G_b + (G_i - G_b)\frac{L}{b}\right] \neq G_i \tag{3.6}$$

for the Model-S0,

$$\int_{-\infty}^{+\infty} \psi_d(x, d, d')\, \mathrm{d}x = \frac{2}{\pi}\left[\left(\frac{\pi}{2} - \tan^{-1}\left[\frac{BG_b}{G_i - (1-B)G_b}\tan\left(\frac{L}{b}\right)\right] + \frac{L}{b}\right)G_b + \frac{G_i - G_b}{B}\frac{L}{b}\right] \neq G_i \tag{3.7}$$

for the Model-S1,

$$\int_{-\infty}^{+\infty} \psi_d(x, d, d')\, \mathrm{d}x = G_i \tag{3.8}$$

for the Model-S2. The integration results w.r.t. various length-scale parameters b, L are visualized in Figure 1 (h), as can be noticed, Model-S0 and Model-S1 have failed to accurately assess the fracture property of a sharp interface. Besides, the integrated fracture energy within the phase-field framework is dependent on length-scale parameters, e.g., significant overestimation is anticipated when L/b is smaller in the Model-S0, similarly, underestimation is expected when L/b is smaller in the Model-S1. However, Model-S2 elaborately determines the effective interface fracture energy $\tilde{G}_i$, so that energetic equivalence between the sharp and diffused representation of interface fracture can be checked and ensured accurately, despite of varying choices of length-scale parameters, which accordingly promises numerical results independent on the choices of length-scale parameters.

The other category from the literature includes Model-E0 and Model-E1, whose interpolation functions are both constructed on the basis of an auxiliary Allen-Cahn (phase-field) indicator, details will be shown later in Section 3.3. In the above 1D setup, we have $A(x) = \exp(-\frac{|x|}{L})$, with the center $x = 0$ exhibiting the effective interface fracture energy $\tilde{G}_i$, smoothly transitioning to the bulk property G_b as depicted in Figure 1 (e) and (f). In the Model-E0, the effective interface fracture energy is assumed to be same as the sharp value $\tilde{G}_i = G_i$, which is similar to the Model-S0; while for the Model-E1, $\tilde{G}_i$ is determined according to the formulation in Model-S1, as plotted in Figure 1 (i). With known $G(x)$, the (equilibrium) phase-field profile $d(x)$ can be (numerically) solved from Euler-Lagrange equation, see Eq. (3.5) for the equation and Figure 1 (e), (f) for the visualization of the solution. Subsequently, phase-field interface fracture energy can be calculated w.r.t varying length-scale parameters (L, b) by substituting the profile $d(x)$ into Eq. (3.2) for the (numerical) integration. As shown in Figure 1 (h), Model-E0 and Model-E1 also fail to assess the interface fracture energy, which differs from the sharp value and exhibits dependency under varying choice of length-scale parameters.

3.2. A new phase-field interface model

In order to address the aforementioned shortcomings in Model-E0 and Model-E1, inspired by Model-S2 and for the first time, we proposed a new phase-field interface model named as Model-E2 in this paper. It employs an effective

Table 1: Comparison of diverse cohesive phase-field interface models with fracture energy $G(x) = A(x)\tilde{G}_i + (1 - A(x))G_b$: check of interface fracture energy and length-scale insensitivity.

CPF interface models	$A(x)$	Effective interface fracture energy $\tilde{G}_i$	$d(x)$	Interface fracture energy check $\int_{-\infty}^{+\infty} \psi_d \, \mathrm{d}x \stackrel{?}{=} G_i$	Length-scale insensitivity check (b, L)
Model-S0 [31, 74, 75]	$A(x) = H(L - \lvert x\rvert)$ H: Heaviside function	$\tilde{G}_i = G_i$	$d(x) = \begin{cases} 1 - \epsilon \sin\left(\frac{\lvert x\rvert}{b}\right), & \text{when } \lvert x\rvert < L \\ 1 - \sin\left(\frac{\lvert x\rvert}{b} + \theta\right), & \text{when } L \le \lvert x\rvert \le \left(\frac{\pi}{2} - \theta\right) b \\ 0, & \text{else} \end{cases}$ ϵ and θ determined by G_b, G_i, b and L †	$\neq$	sensitive
Model-S1 [27, 28, 77]	$A(x) = H(L - \lvert x\rvert)$	$\tilde{G}_i = [G_i - (1 - B)G_b]/B$ with $B = \frac{1}{\pi}\left[\frac{2L}{b} + \sin\left(\frac{2L}{b}\right)\right]$	$d(x) = \begin{cases} 1 - \tilde{\epsilon} \sin\left(\frac{\lvert x\rvert}{b}\right), & \text{when } \lvert x\rvert < L \\ 1 - \sin\left(\frac{\lvert x\rvert}{b} + \tilde{\theta}\right), & \text{when } L \le \lvert x\rvert \le \left(\frac{\pi}{2} - \tilde{\theta}\right) b \\ 0, & \text{else} \end{cases}$ $\tilde{\epsilon}$ and $\tilde{\theta}$ determined by G_b, $\tilde{G}_i$, b and L †	$\neq$	sensitive
Model-S2 [29, 76]	$A(x) = H(L - \lvert x\rvert)$	$\tilde{G}_i$ solved from * $\frac{L}{b}\frac{\tilde{G}_i}{G_b} + \frac{\pi}{2}\left(1 - \frac{G_i}{G_b}\right)$ $- \tan^{-1}\left[\frac{G_b}{\tilde{G}_i}\tan\left(\frac{L}{b}\right)\right] = 0$	$d(x) = \begin{cases} 1 - \tilde{\epsilon} \sin\left(\frac{\lvert x\rvert}{b}\right), & \text{when } \lvert x\rvert < L \\ 1 - \sin\left(\frac{\lvert x\rvert}{b} + \tilde{\theta}\right), & \text{when } L \le \lvert x\rvert \le \left(\frac{\pi}{2} - \tilde{\theta}\right) b \\ 0, & \text{else} \end{cases}$ $\tilde{\epsilon}$ and $\tilde{\theta}$ determined by G_b, $\tilde{G}_i$, b and L †	$=$	insensitive
Model-E0 [18, 20]	$A(x) = \exp\left(-\frac{\lvert x\rvert}{L}\right)$	$\tilde{G}_i = G_i$	solved from $\frac{\partial \psi_d}{\partial d} - \frac{\mathrm{d}}{\mathrm{d}x}\left(\frac{\partial \psi_d}{\partial d'}\right) = 0$ with given $\psi_d = [\exp(-\lvert x\rvert/L)G_i + (1 - \exp(-\lvert x\rvert/L))\, G_b]\, \gamma(d, d')$	$\neq$	sensitive
Model-E1 [21, 22]	$A(x) = \exp\left(-\frac{\lvert x\rvert}{L}\right)$	$\tilde{G}_i = [G_i - (1 - B)G_b]/B$ with $B = \frac{1}{\pi}\left[\frac{2L}{b} + \sin\left(\frac{2L}{b}\right)\right]$	solved from $\frac{\partial \psi_d}{\partial d} - \frac{\mathrm{d}}{\mathrm{d}x}\left(\frac{\partial \psi_d}{\partial d'}\right) = 0$ with given $\psi_d = \left[\exp(-\lvert x\rvert/L)\tilde{G}_i + (1 - \exp(-\lvert x\rvert/L))\, G_b\right]\gamma(d, d')$	$\neq$	sensitive
Model-E2 (currently proposed)	$A(x) = \exp\left(-\frac{\lvert x\rvert}{L}\right)$	$\tilde{G}_i, d(x)$ solved from $\begin{cases} \int_{-\infty}^{+\infty} \psi_d \, \mathrm{d}x = G_i \\ \frac{\partial \psi_d}{\partial d} - \frac{\mathrm{d}}{\mathrm{d}x}\left(\frac{\partial \psi_d}{\partial d'}\right) = 0 \end{cases}$ with $\psi_d = \left[\exp(-\lvert x\rvert/L)\tilde{G}_i + (1 - \exp(-\lvert x\rvert/L))\, G_b\right]\gamma(d, d')$		$=$	insensitive

† $\tilde{\epsilon} = 1/\sqrt{\sin^2\left(\frac{L}{b}\right) + \frac{\tilde{G}_i}{G_b} \cdot \cos^2\left(\frac{L}{b}\right)}$ and $\tilde{\theta} = \tan^{-1}\left[\frac{G_b}{\tilde{G}_i}\tan\left(\frac{L}{b}\right)\right] - \frac{L}{b}$ for the corresponding $\tilde{G}_i$ defined in different models. In Model-S0, $\tilde{\epsilon} = \epsilon, \tilde{\theta} = \theta$ for $\tilde{G}_i = G_i$.

* Simplified from $\int_{-\infty}^{+\infty} \psi_d \, \mathrm{d}x = G_i$, with $\psi_d = \left[H(L - \lvert x\rvert)\tilde{G}_i + (1 - H(L - \lvert x\rvert))\, G_b\right]\gamma(d, d')$.

interface fracture energy $\tilde{G}_i$ in the exponential $G(x)$, which is solved on the basis of the Euler-Lagrange equation of the phase-field theory and the interface energy consistency w.r.t. that of the cohesive zone model.

The fracture energy distribution in the 1D-domain is given as following,

$$G(x) = \exp\left(-\frac{|x|}{L}\right)\tilde{G}_i + \left(1 - \exp\left(-\frac{|x|}{L}\right)\right)G_b, \tag{3.9}$$

where the effective interface fracture energy $\tilde{G}_i$ is to be determined from the consistent surface energy constraint. Meanwhile, the phase-field profile $d(x)$ can be (numerically) solved according to the Euler-Lagrange equation under above $G(x)$. Accordingly, the unknown scalar $\tilde{G}_i$ and the unknown variable $d(x)$ can be simultaneously determined by solving following coupled equations,

$$\begin{cases} \displaystyle\int_{-\infty}^{+\infty} \psi_d(x, d, d')\ \mathrm{d}x = G_i \\ \dfrac{\partial \psi_d}{\partial d} - \dfrac{\mathrm{d}}{\mathrm{d}x}\left(\dfrac{\partial \psi_d}{\partial d'}\right) = 0, \quad \text{subjected to } \ \dot{d} \geq 0,\ d(x=0) = 1 \text{ and } d(x = \pm\infty) = 0 \end{cases} . \tag{3.10}$$

In order to solve the equation system in Eq. (3.10), which consists of a transcendental equation (TE) in integral form for the unknown effective interface fracture energy $\tilde{G}_i$, along with a partial differential equation (PDE) for the unknown phase-field variable $d(x)$, we adopt a staggered algorithm to sequentially and iteratively solve two coupled equations, e.g., an initially trail value $\tilde{G}_i = \tilde{G}_{i0} \in [0, G_i]$ is set to start the iteration, then profile $d(x)$ can be obtained by solving the PDE using the finite-element method under given $G(x)$, next, the bisection method properly bisecting the original interval $[0, G_i]$ to the updated one, e.g., $\left[0, \tilde{G}_{i0}\right]$ when $\int_{-\infty}^{+\infty} \psi_d(x, d, d')\ \mathrm{d}x > G_i$ or $\left[\tilde{G}_{i0}, G_i\right]$ when $\int_{-\infty}^{+\infty} \psi_d(x, d, d')\ \mathrm{d}x < G_i$ with $\tilde{G}_i = \tilde{G}_{i0}$ plugged in, is applied to the TE. Aforementioned procedures consisting of staggered iterations and bisecting the interval are repeated, until the length of the updated interval for $\tilde{G}_i$ in the bisection method meets the defined threshold.

As plotted in Figure 1 (g), the spatial distribution of fracture energy $G(x)$ with $\tilde{G}_i$ and the corresponding phase-field variable $d(x)$ are illustrated. Besides, $\tilde{G}_i$ obtained from above coupled equations in terms of varying length-scale parameters b and L under the condition $G_i = 0.5G_b$ is illustrated in Figure 1 (i). Figure 1 (h) plotted the integrated phase-field fracture energy under varying L/b, which is constrained with energy equivalence to that of a sharp interface. It can be concluded that, Model-E2, which employs a diffusive exponential representation of the interface additionally equipped with an elaborately determined effective interface fracture energy, establishes equivalence to a sharp interface crack in terms of fracture energy dissipation. Consequently, the proposed model anticipates the advantageous insensitivity to length-scale parameters (b and L).

Remark 1 It is noteworthy to highlight that, the diffusive representation of an interface equipped with an elaborately determined effective interface fracture energy is a rather robust approach for phase-field modeling of interface fracture, and its applicability is not confined to the specific types of interpolation functions as previously discussed, e.g., stair-wise function $A(x) = H(x)$ and exponential one $A(x) = \exp(-\frac{|x|}{L})$, as it extends to encompass a more general representation of the interface, such as the parabolic one in [78], which can be constructed by properly defining $A(x)$

in Eq. (3.1) and correspondingly solving the effective interface fracture energy $\tilde{G}_i$ according to the interface energy consistency. □

Remark 2 As for the crack surface energy density functional $\psi_d(x, d, d')$ in Eq. (3.2) for interface fracture, when the fracture energy of bulk material is assigned over the whole domain, i.e., $G(x) = G_b$, the density functional $\psi_d^b(d, d')$ in Eq. (2.1) for the bulk fracture can be recovered. In the following section of the manuscript, $\psi_d(x, d, d')$ in the unified form is employed, which can potentially model both interface and bulk fractures. □

3.3. Implementation of the proposed phase-field interface model under multi-dimensional case

In this section, the proposed phase-field interface model is extended to multi-dimensional cases. The crack phase-field variable reads $d(\boldsymbol{x}) : \Omega \in [0, 1]$, with $\boldsymbol{x}$ labeling the spatial coordinate in 2D/3D setup, and the corresponding crack surface energy density functional is defined as following,

$$\psi_d(\boldsymbol{x}, d, \nabla d) = G(\boldsymbol{x})\, \gamma(d, \nabla d), \qquad \text{with} \qquad \gamma(d, \nabla d) = \frac{1}{\pi}\left(\frac{2d - d^2}{b} + b|\nabla d|^2\right), \tag{3.11}$$

where $\gamma(d, \nabla d)$ is expressed in terms of phase-field variable and its spatial gradient, $G(\boldsymbol{x})$ is the fracture energy distribution in the domain. In this case, the distribution of fracture energy $G(\xi)$ and the corresponding phase-field profile $d(\xi)$ along the normal direction of interfaces adhere to the configurations established in the preceding 1D case, as can be seen in Figure 2 (b) and (c), here ξ denotes the normal distance away from the interface in the local coordinate system.

In order to numerically implement the interpolation of fracture energy between the bulk value G_b and the effective interface value $\tilde{G}_i$, we introduce an auxiliary (phase-field) indicator $\eta(\boldsymbol{x})$ to diffusively represent the interface, with following Allen-Cahn type governing equation [18, 79] and boundary conditions adopted to solve the spatial distribution of the indicator $\eta(\boldsymbol{x})$,

$$\begin{cases} \eta(\boldsymbol{x}) - L^2\eta''(\boldsymbol{x}) = 0, & \text{in } \Omega \\ \nabla\eta \cdot \boldsymbol{n} = 0, & \text{on } \partial\Omega \end{cases}, \qquad \text{subjected to } \ \eta(\boldsymbol{x} \in \Gamma) = 1, \tag{3.12}$$

where Ω denotes the 2D/3D domain whose external boundary $\partial\Omega$ has outward unit normal vector $\boldsymbol{n}$, Γ represents the location of sharp interface (see Figure 2 (a)), L is the length-scale parameter regularizing the interface and it controls the varying slope of interface indicator. With the interface indicator $\eta(\boldsymbol{x})$ at hands (see Figure 2 (b) for the visualization), the fracture energy in the domain can be formulated as [18, 20]

$$G(\boldsymbol{x}) = \eta(\boldsymbol{x})\tilde{G}_i + (1 - \eta(\boldsymbol{x}))\, G_b, \tag{3.13}$$

as shown in Figure 2 (c), the position at the sharp interface exhibits effective interface fracture energy $\tilde{G}_i$, smoothly transitioning to the bulk property G_b. At the normal direction of the interface, we have the indicator distribution expressed w.r.t. ξ in local coordinate system

$$\eta(\xi) = \exp(-\frac{|\xi|}{L}), \tag{3.14}$$

by plugging in, we have the fracture energy distribution at the interface normal direction

$$G(\xi) = \exp\left(-\frac{|\xi|}{L}\right)\tilde{G}_i + \left(1 - \exp\left(-\frac{|\xi|}{L}\right)\right)G_b, \tag{3.15}$$

which is visualized in the Figure 2 (c), and it aligns precisely with the prior 1D configuration presented in Eq. (3.9).

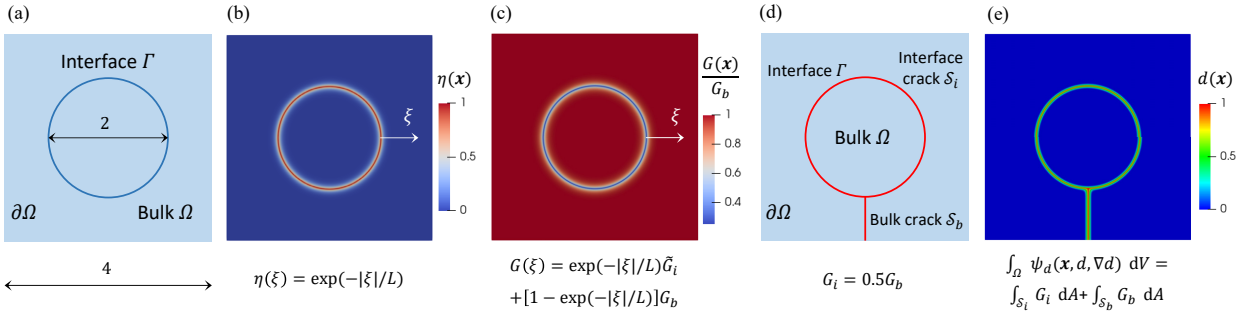

Figure 2: Illustrations of numerical implementation of the proposed phase-field interface model under 2D case. Figure (a) shows the square domain with bulk phase Ω and embedded circular interface Γ. Figure (b) and (c) respectively show the profiles of indicator variable $\eta(\boldsymbol{x})$ and fracture energy $G(\boldsymbol{x})$ (normalized with G_b), besides, the distributions at the interface normal direction are also shown. Figure (d) illustrates the bulk crack $\mathcal{S}_b$ with quarter specimen's length and surface energy G_b, and the sharp interface crack $\mathcal{S}_i$ which is overlapped with the interface and has fracture energy $G_i = 0.5G_b$. Figure (e) shows the crack phase-field profile. $L = 0.04$ and $b = 0.05$ are adopted in the regularization, leading to $\tilde{G}_i = 0.5084G_i$; the energy consistence between the phase-field diffusive approach and the sharp value can be numerically checked here. Although this illustration is shown in 2D, the model and numerical implementation are applicable to 3D simulations, as shown in Figure 10.

Here we present a 2D example to validate the aforementioned numerical implementation. As shown in Figure 2 (a) and (d), square-shape bulk region Ω with embedded circular sharp interface Γ is considered in the domain, sharp interface crack $\mathcal{S}_i$ spatially overlapped with Γ and bulk crack $\mathcal{S}_b$ of quarter specimen's length are assumed to occur. From the numerical validation in Figure 2 (e), we can conclude following constructed energy consistence between the proposed phase-field framework and the cohesive zone model,

$$\int_\Omega \psi_d(\boldsymbol{x}, d, \nabla d)\, \mathrm{d}V = \int_{\mathcal{S}_i} G_i\, \mathrm{d}A + \int_{\mathcal{S}_b} G_b\, \mathrm{d}A, \tag{3.16}$$

which covers the energy dissipation for concurrent bulk and interface fractures.

4. Chemo-mechanical cohesive phase-field model for inter- and trans-granular fractures

On the basis of the proposed phase-field interface model, in this section, we extend its applicability to chemo-mechanical cohesive fracture in general multi-dimensional case in a thermodynamically consistent manner. Note in this chapter for mathematical formulation, scalars are denoted by italic light-face Greek or Latin letters (e.g., c or λ); vectors, second- and fourth-order tensors are signified by italic boldface minuscule, majuscule and blackboard-bold majuscule characters like $\boldsymbol{q}$, $\boldsymbol{D}$ and $\mathbb{E}$, respectively.

As shown in Figure 3 (a), let $\Omega \subset \mathbb{R}^{n_{\text{dim}}}$ ($n_{\text{dim}} = 1, 2, 3$) be the reference configuration of heterogeneous polycrystalline solid with multiple grains and GBs, its external boundary is denoted by $\partial\Omega \subset \mathbb{R}^{n_{\text{dim}}-1}$ with the outward normal

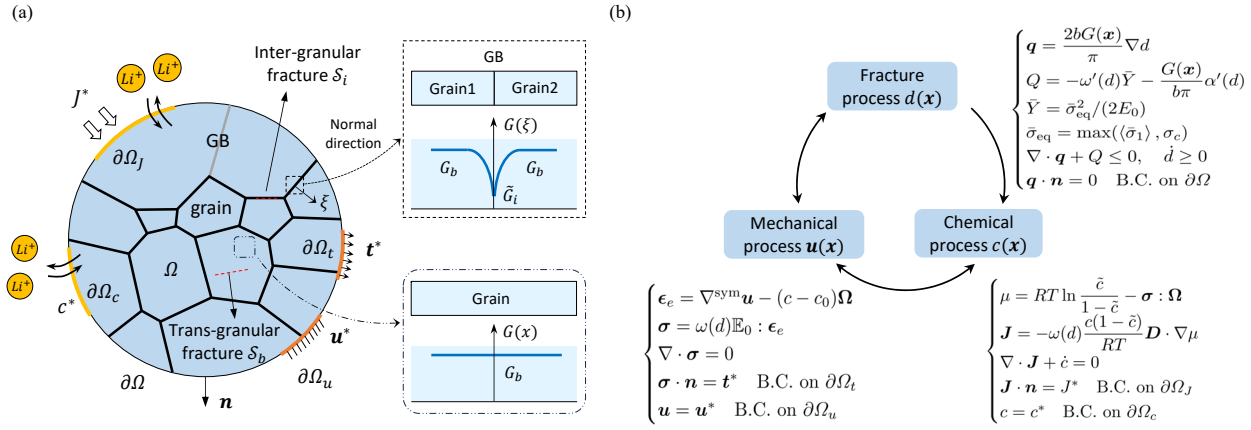

Figure 3: Illustrations of cohesive phase-field model for chemo-mechanical fractures in a NMC polycrystalline particle. Figure (a) presents a typical microstructure of NMC particle with multiple grains and GBs. The boundary conditions for both chemical and mechanical sub-problems are illustrated, possible crack patterns including inter- and trans- granular fracture are also provided. The distribution of the fracture energy $G(x)$ in the diffusively represented GB (utilizing the newly proposed Model-E2) and the bulk material are highlighted in the zoomed call-out. Although this illustration is shown in 2D, models in this chapter are applicable to 3D simulations. Figure (b) shows the chemical-mechanical-fracture coupled formulations and the couplings of different physics.

vector $\boldsymbol{n}$. Two different fracture modes, i.e., inter-granular fracture $\mathcal{S}_i$ at the grain boundary and trans-granular fracture $\mathcal{S}_i$ within the grain, can be observed in the figure.

4.1. Kinematics and chemo-mechanical governing equations

As also can be seen in Figure 3 (a), the chemo-mechanical behaviors of NMC particle are characterized by the displacement (vector) field $\boldsymbol{u}(\boldsymbol{x}, t)$ and the concentration (scalar) field $c(\boldsymbol{x}, t)$, in addition to phase-field crack $d(\boldsymbol{x})$, with $\boldsymbol{x}$ and t labeling the material point and time, respectively. Under the small-deformation setting, the total strain tensor $\boldsymbol{\epsilon}(\boldsymbol{x})$ is obtained via the symmetric part of the displacement gradient tensor, which can be further decomposed into two parts, i.e., elastic $\boldsymbol{\epsilon}_e$ and chemical $\boldsymbol{\epsilon}_c$ strain tensors.

$$\boldsymbol{\epsilon} = \nabla^{\text{sym}}\boldsymbol{u} = \frac{1}{2}(\nabla\boldsymbol{u} + \nabla^{\text{T}}\boldsymbol{u}) = \boldsymbol{\epsilon}_e + \boldsymbol{\epsilon}_c, \tag{4.1a}$$

$$\boldsymbol{\epsilon}_c = (c - c_0)\boldsymbol{\Omega}, \qquad \boldsymbol{\Omega} = \Omega_{ij}\boldsymbol{e}_i \otimes \boldsymbol{e}_j. \tag{4.1b}$$

The elastic part directly contributes to the mechanical stress, while the chemical one measures the material volume change induced by varying concentration within the host material during (dis)charging processes. Here c_0 denotes the initial concentration in the active material under stress-free state; $\boldsymbol{\Omega}$ is the chemical deformation (swelling/shrinkage) tensor determining lithium-concentration-dependent volume change, its components are represented by the partial molar volume Ω_{ij}.

In the mechanically quasi-static case (body force is ignored) under consideration, the mechanical stress tensor $\boldsymbol{\sigma}$

and the chemical flux $\boldsymbol{J}$ in the current configuration are governed by the following equations:

$$\begin{cases} \nabla \cdot \boldsymbol{\sigma} = \boldsymbol{0} & \text{in } \Omega \\ \boldsymbol{\sigma} \cdot \boldsymbol{n} = \boldsymbol{t}^* & \text{on } \partial\Omega_t \\ \boldsymbol{u} = \boldsymbol{u}^* & \text{on } \partial\Omega_u \end{cases}, \tag{4.2a}$$

$$\begin{cases} \nabla \cdot \boldsymbol{J} + \dot{c} = 0 & \text{in } \Omega \\ \boldsymbol{J} \cdot \boldsymbol{n} = J^* & \text{on } \partial\Omega_J \\ c = c^* & \text{on } \partial\Omega_c \end{cases}. \tag{4.2b}$$

Here prescribed traction force $\boldsymbol{t}^*$ (on $\partial\Omega_t$) and displacement $\boldsymbol{u}^*$ (on $\partial\Omega_u$) are boundary conditions on the external surface $\partial\Omega$ for mechanical sub-problem; chemical flux J^* and concentration c^* applied on surfaces $\partial\Omega_J$ and $\partial\Omega_c$, respectively, serve as chemical boundary conditions, in order to mimic the electrochemical responses and lithium (de)intercalation flux on the interface between electrolyte and electrode particles [68, 74].

4.2. Thermodynamic and dissipation inequality

Under chemo-mechanical-fracture coupled circumstance, the constitutive laws of all processes and the governing equation of crack phase-field are derived in a thermodynamically consistent manner. Consider an isothermal and adiabatic system, the second law of thermodynamics dictates that, in its global formulation, the interplay between external power and internal potential energy entails an energy dissipation rate that demands non-negative, i.e.,

$$\dot{\mathscr{D}} = \int_{\partial\Omega} \boldsymbol{t}^* \cdot \dot{\boldsymbol{u}} \, \mathrm{d}A - \int_{\partial\Omega} J^* \mu \, \mathrm{d}A - \int_{\Omega} \dot{\psi} \, \mathrm{d}V \geq 0, \tag{4.3}$$

where time derivation is denoted by $\dot{()}$, μ is the chemical potential, and ψ represents internal potential energy density taking into account the contributions from all processes including chemical, mechanical and fracture sub-problems,

$$\psi = \psi_c(c) + \psi_m(\boldsymbol{\epsilon}(\boldsymbol{u}), c, d) + \psi_d(\boldsymbol{x}, d, \nabla d), \tag{4.4a}$$

$$\psi_c = RTc_{\max}[\tilde{c} \ln \tilde{c} + (1 - \tilde{c}) \ln(1 - \tilde{c})], \tag{4.4b}$$

$$\psi_m = \frac{1}{2} \boldsymbol{\epsilon}_e : \omega(d) \mathbb{E}_0 : \boldsymbol{\epsilon}_e = \frac{1}{2} (\boldsymbol{\epsilon} - \boldsymbol{\epsilon}_c) : \omega(d) \mathbb{E}_0 : (\boldsymbol{\epsilon} - \boldsymbol{\epsilon}_c), \tag{4.4c}$$

together with crack surface energy density functional $\psi_d(\boldsymbol{x}, d, \nabla d)$ defined in Eq. (3.11). In above formulations, R is the gas constant, T is the reference temperature, $c_{\max}$ denotes the maximum Li concentration in active material for normalizing Li concentration $\tilde{c} = c/c_{\max}$, $\mathbb{E}_0 = \lambda_0 \mathbf{1} \otimes \mathbf{1} + \mu_0 \mathbb{I}$ is the fourth-order isotropic elasticity tensor, where $\mathbf{1}$ and $\mathbb{I}$ are the unit second- and fourth- order tensors, respectively, $\lambda_0 = \nu_0 E_0/[(1 - 2\nu_0)(1 + \nu_0)]$ and $\mu_0 = E_0/[2(1 + \nu_0)]$ are the Lamé constants of isotropic elasticity, expressed in terms of Young's modulus E_0 and Poisson's ratio ν_0 of the material. The energetic degradation function $\omega(d)$ in the cohesive phase-field fracture model [13] is expressed in terms of crack phase-field d as following,

$$\omega(d) = \frac{(1 - d)^2}{(1 - d)^2 + a_1 d(1 - 0.5d)}, \quad \text{with} \quad a_1 = \frac{4 l_{\text{ch}}}{\pi b}, \tag{4.5}$$

where $l_{\text{ch}} = \bar{E}_0 G(\boldsymbol{x})/\sigma_c^2$ is the Irwin's internal length [13, 80], and σ_c is the failure strength (critical stress) under uni-axial tensile test, $\bar{E}_0 = E_0(1-\nu_0)/(1+\nu_0)/(1-2\nu_0)$ expresses the longitudinal modulus. It's worth noting that, as an initial attempt to apply the proposed phase-field interface model for simulating complex fracture behaviors in polycrystalline structures, we have simplified the model by assuming isotropic elastic properties and fracture energy following the approach of studies such as [81, 82], while only considered anisotropic chemical deformation tensor and diffusivity (see Eq. (5.2)). In future work, we plan to extend this model to incorporate transversely isotropic material properties to better capture the mechanical behavior of polycrystalline cathode particles with layered structures, including the grain-orientation-dependent fracture energy, as discussed in [19, 24, 83–85].

By inserting the variations of Eq. (4.4) into Eq. (4.3), we can obtain

$$\dot{\mathscr{D}} = \int_\Omega \left(\boldsymbol{\sigma} - \frac{\partial \psi}{\partial \boldsymbol{\epsilon}}\right) : \dot{\boldsymbol{\epsilon}}\, \mathrm{d}V + \int_\Omega \left(\mu - \frac{\partial \psi}{\partial c}\right)\dot{c}\, \mathrm{d}V - \int_\Omega \boldsymbol{J}\cdot\nabla\mu\, \mathrm{d}V - \int_\Omega \left(\frac{\partial \psi}{\partial d}\dot{d} + \frac{\partial \psi}{\partial \nabla d}\cdot\nabla\dot{d}\right)\mathrm{d}V \geq 0, \tag{4.6}$$

follow the Coleman-Noll principle [86] for satisfying the dissipation inequality, coupled chemo-mechanical constitutive equations can be obtained:

$$\boldsymbol{\sigma} = \frac{\partial \psi}{\partial \boldsymbol{\epsilon}} = \frac{\partial \psi_m}{\partial \boldsymbol{\epsilon}} = \omega(d)\mathbb{E}_0 : (\boldsymbol{\epsilon} - \boldsymbol{\epsilon}_c)\,, \tag{4.7a}$$

$$\mu = \frac{\partial \psi}{\partial c} = \frac{\partial \psi_c}{\partial c} + \frac{\partial \psi_m}{\partial c} = RT\ln\frac{\tilde{c}}{1-\tilde{c}} - \boldsymbol{\sigma} : \boldsymbol{\Omega}, \tag{4.7b}$$

$$\boldsymbol{J} = -\boldsymbol{M}(c,d)\cdot\nabla\mu = -\omega(d)\frac{c(1-\tilde{c})}{RT}\boldsymbol{D}\cdot\nabla\mu. \tag{4.7c}$$

In above formulations, $\boldsymbol{M} = \omega(d)c(1-\tilde{c})/(RT)\boldsymbol{D}$ is concentration-dependent mobility tensor, which is degraded by $\omega(d)$ in terms of crack phase-field; $\boldsymbol{D} = D_{ij}\boldsymbol{e}_i \otimes \boldsymbol{e}_j$ denotes the diffusivity tensor with D_{ij} representing its components. As can be seen from the thermodynamic derivations, chemical potential Eq. (4.7b) and chemical flux Eq. (4.7c) is affected by both the gradients of lithium concentration and mechanical stress. Under above settings of flux vector $\boldsymbol{J}$ with linearly dependence on the gradient of chemical potential $\nabla\mu$, following term in Eq. (4.6) can be ensured non-negative, e.g.,

$$-\int_\Omega \boldsymbol{J}\cdot\nabla\mu\, \mathrm{d}V = \int_\Omega \omega(d)\frac{c(1-\tilde{c})}{RT}\boldsymbol{D}\cdot\nabla\mu\cdot\nabla\mu\, \mathrm{d}V \geq 0. \tag{4.8}$$

The remaining term in the dissipation inequality Eq. (4.6) after employing partial integration reads:

$$\int_\Omega \left[-\omega'(d)\bar{Y} - \frac{G(\boldsymbol{x})}{b\pi}(2-2d) + \frac{2b}{\pi}G(\boldsymbol{x})\nabla\cdot\nabla d\right]\dot{d}\, \mathrm{d}V + \int_{\partial\Omega} -\frac{2b}{\pi}G(\boldsymbol{x})\boldsymbol{n}\cdot\nabla d\, \dot{d}\, \mathrm{d}A \;\geq 0. \tag{4.9}$$

Call for the dissipative nature of damage evolution, i.e., $\dot{d} \geq 0$, by assuming the maximum dissipation principle and applying the Lagrange multipliers under Karush–Kuhn–Tucker (KKT) constraints, we obtain following governing equations for the crack phase-field,

$$\begin{cases} Q + \nabla\cdot\boldsymbol{q} = 0, & \text{when } \dot{d} > 0 \quad \text{in } \Omega \\ Q + \nabla\cdot\boldsymbol{q} < 0, & \text{when } \dot{d} = 0 \quad \text{in } \Omega \\ \nabla d\cdot\boldsymbol{n} = 0 & \text{on } \partial\Omega \end{cases}, \quad \text{with} \quad \begin{cases} Q = -\omega'(d)\bar{Y} - \dfrac{G(\boldsymbol{x})}{b\pi}(2-2d) \\ \boldsymbol{q} = \dfrac{2b}{\pi}G(\boldsymbol{x})\nabla d \end{cases}, \tag{4.10}$$

with the crack driving force expressed as $\bar{Y} = \frac{1}{2}(\boldsymbol{\epsilon} - \boldsymbol{\epsilon}_c) : \mathbb{E}_0 : (\boldsymbol{\epsilon} - \boldsymbol{\epsilon}_c)$ from the thermodynamically consistent derivation.

The aforementioned driving force does not distinguish between the asymmetric mechanical responses of solids under tension and compression. To prevent the fracture and damage to happen under compressive state, one may utilize either positive/negative [12] or volumetric/deviatoric [11] decomposition of the strain, stress or effective stress, as extensively discussed in [87, 88]. A simpler solution [89, 90] is to maintain isotropic stress-strain relation Eq. (4.7a) while consider contribution from positive effective stress in the mechanical driving force, i.e.,

$$\bar{Y} = \frac{1}{2}\boldsymbol{\epsilon}_e : \mathbb{E}_0 : \boldsymbol{\epsilon}_e = \frac{1}{2}\bar{\boldsymbol{\sigma}} : \mathbb{S}_0 : \bar{\boldsymbol{\sigma}} \qquad \Longrightarrow \qquad \bar{Y} = \frac{1}{2}\bar{\boldsymbol{\sigma}}^+ : \mathbb{S}_0 : \bar{\boldsymbol{\sigma}}^+, \tag{4.11}$$

where $\mathbb{S}_0$ is the compliance fourth-order tensor in mechanical sub-problem, and effective stress is defined as $\bar{\boldsymbol{\sigma}} = \mathbb{E}_0 : \boldsymbol{\epsilon}_e = \mathbb{E}_0 : (\boldsymbol{\epsilon} - \boldsymbol{\epsilon}_c)$. In this work, the positive/negative projection of the effective stress in energy norm [89] is adopted, with the positive cone expressed as $\overline{\boldsymbol{\sigma}}^+ = \sum_{i=1}^{3} \bar{\sigma}_i^+ \boldsymbol{v}_i \otimes \boldsymbol{v}_i$, for the i-th principal value $\bar{\sigma}_i^+$ and the corresponding principal vector $\boldsymbol{v}_i$ of the effective stress tensor $\bar{\boldsymbol{\sigma}}$. For simplicity, this work exclusively considers the simplest case, wherein crack evolution is driven solely by its major principal value [89, 90], thus,

$$\bar{Y} = \frac{\bar{\sigma}_{\text{eq}}^2}{2\bar{E}_0}, \qquad \text{with} \quad \bar{\sigma}_{\text{eq}} = \max(\langle \bar{\sigma}_1 \rangle, \sigma_c). \tag{4.12}$$

In the above, the Macaulay brackets $\langle \cdot \rangle$ are defined as $\langle x \rangle = \max(x, 0)$, and σ_c means uni-axial tensile strength as mentioned before. By redefining the crack driving force $\bar{Y}$, it becomes feasible to effectively capture tension-dominant fracture behaviors in cathode particles. It's worth noting that while such modifications and the aforementioned constitutive relations may not be variationally consistent, they do uphold thermodynamic consistency in terms of energy dissipation [89].

4.3. Summary of chemo-mechanical cohesive phase-field fracture model

The governing equations, constitutive equations and boundary conditions of chemo-mechanical cohesive phase-field fracture model are summarized in Figure 3 (b), wherein the displacement field $\boldsymbol{u}(\boldsymbol{x})$, lithium concentration field $c(\boldsymbol{x})$, and crack phase-field $d(\boldsymbol{x})$ serve as primary unknowns in the mechanical, chemical, and fracture sub-problems, respectively.

The couplings of different physics are also shown in Figure 3 (b), as can be seen, chemical and mechanical processes are fully coupled, i.e., changing lithium concentration leads to chemical deformation and mechanical stress, which conversely influences the distribution of lithium concentration. Meanwhile, mechanical and fracture processes exhibit a two-way coupled relationship, e.g., mechanical stress drives the evolution of cracks and fractures, which conversely damage the structural integrity and degrade its bearing capacity. Additionally, the fracture process exerts an influence on the chemical sub-problem, specifically, through the degradation of diffusivity with the presence of crack, which obstructs the transport of lithium; while the direct effect of chemical process on fracture sub-problem is not integrated into the current framework, which can be extended in our future work by considering concentration-dependent fracture property [74, 81] or cycles induced materials' embrittlement [54].

5. Numerical examples and results

In this section, a series of numerical examples regarding bulk (trans-granular) and interface (inter-granular) fractures in purely-mechanical and chemo-mechanical problems are simulated using the proposed model. Firstly, purely-mechanical benchmark examples are presented, to demonstrate the capability of the proposed model to investigate the competition between the interface delamination and crack penetration into the bulk, besides, the merit of length-scale insensitivity is also addressed. Secondly, for validating the applicability to chemo-mechanically coupled scenario, similar specimens under chemical delithiation mimicking the charging condition of cathode particles are considered. The competition between interface delamination and bulk fracture is also investigated under chemo-mechanical case, meanwhile, the independence of numerically predicted results on phase-field and interface length-scale parameters (b and L) is emphasized by comparison with various models. Moreover, predictions given by cohesive phase-field fracture model are compared and validated with results by the cohesive zone model (see Appendix B for formulations). Eventually, the proposed model is applied to image-based reconstructed 3D polycrystalline geometry, simulating its diverse (inter-/trans- granular) fracture patterns in NMC cathode particles.

The cohesive phase-field fracture models (under both purely-mechanical and chemo-mechanical circumstances) are implemented into the open-source FEM framework Multiphysics Object-Oriented Simulation Environment (MOOSE, `https://mooseframework.inl.gov/index.html`). The geometry and finite-element meshes of benchmark examples are generated with the aid of the open-source software Gmsh (`https://gmsh.info/`). Finally, the visualization of obtained results are carried out on ParaView (`https://www.paraview.org/`). The utilization of energy degradation function in Eq. (4.5) in the CPF model necessitates the fulfillment of its convexity w.r.t. phase-field variable, thereby imposing specific criterion on the value of phase-field length-scale b. Besides, the element size h and the phase-field length-scale b satisfy $h \leq b/3$, in order to resolve the gradient of the crack phase-field. Interested readers can refer to [31, 80] for details.

5.1. Purely-mechanical benchmark: Crack impinging on an interface

This example aims to investigate the competition between deflection and penetration of a crack, which impinges on an interface. As Figure 4 (a) shows, we consider a rectangular computational domain of 1 mm $\times$ 2 mm, with a straight horizontal notch at the middle height and an internal interface of inclined angle θ from the horizontal axis introduced in the specimen. The bottom edge is mechanically fixed, while a vertical displacement is applied on the top edge.

The parameters adopted in the simulation are listed in Table 2, in particular, the interface has weaker mechanical failure resistance, i.e., lower fracture energy $G_i = 0.6G_b$ is adopted. According to linear elastic fracture mechanics (LEFM), the critical ratio between the fracture energy of the sharp interface and the bulk phase, which determines a crack to deflect along the interface or penetrate into the bulk, can be expressed as a function of the inclined angle $f(\theta)$

Table 2: Material parameters in the purely-mechanical example taken from [13, 15, 27]

Material parameters	Value	Unit
Young's modulus E_0	210	[GPa]
Poisson's ratio ν_0	0.3	[-]
Bulk tensile strength $\sigma_{c,b}$	2400	[MPa]
Interface tensile strength $\sigma_{c,i}$	1536	[MPa]
Bulk fracture energy G_b	2700	[N/m]
Interface fracture energy G_i	1620	[N/m]

[91, 92],

$$f(\theta) = \frac{1}{16}\left[\left(3\cos\frac{\theta}{2} + \cos\frac{3\theta}{2}\right)^2 + \left(\sin\frac{\theta}{2} + \sin\frac{3\theta}{2}\right)^2\right], \tag{5.1}$$

e.g., the crack deflects into the interface when $\frac{G_i}{G_b} < f(\theta)$, otherwise the crack penetrates into the bulk phase. In the simulation, we fixed the fracture energy of bulk phase and the interface, while three different angles $\theta = 30°, 45°, 60°$ are considered for comparison.

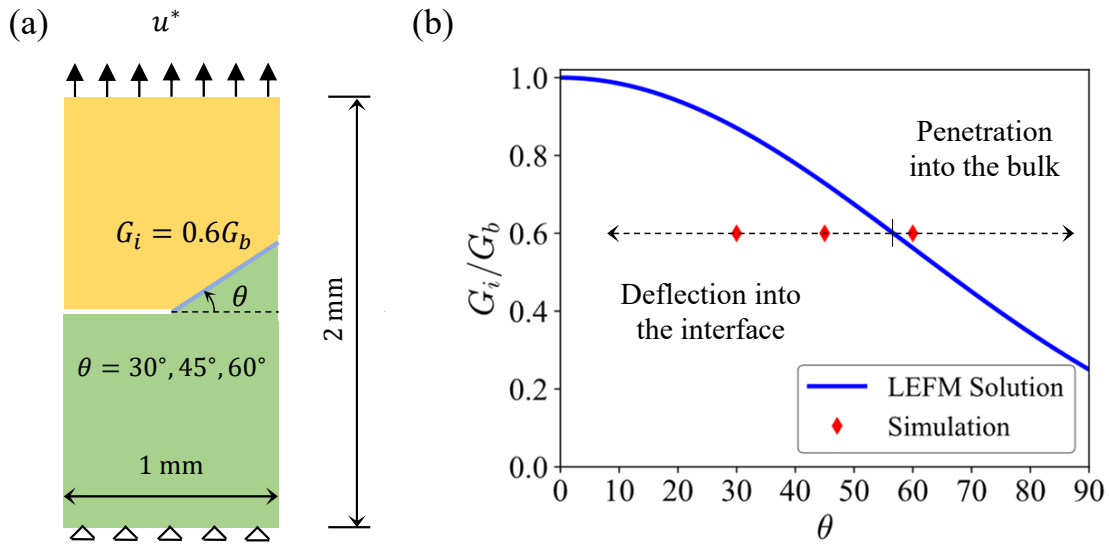

Figure 4: Schematic view of a crack impinging on an interface (left), and the predictions of deflection and penetration at various inclination angles (θ) comparing analytical results from Linear Elastic Fracture Mechanics (LEFM) [91, 92] and phase-field simulations based on the proposed model (right).

As shown in Figure 4 (b) and Figure 5, for smaller inclined angles such as $\theta = 30°, 45°$, the cracks initiate with further propagation at the interface, where the criterion $\frac{G_i}{G_b} = 0.6 < f(\theta)$ is met; while for $\frac{G_i}{G_b} = 0.6 >$

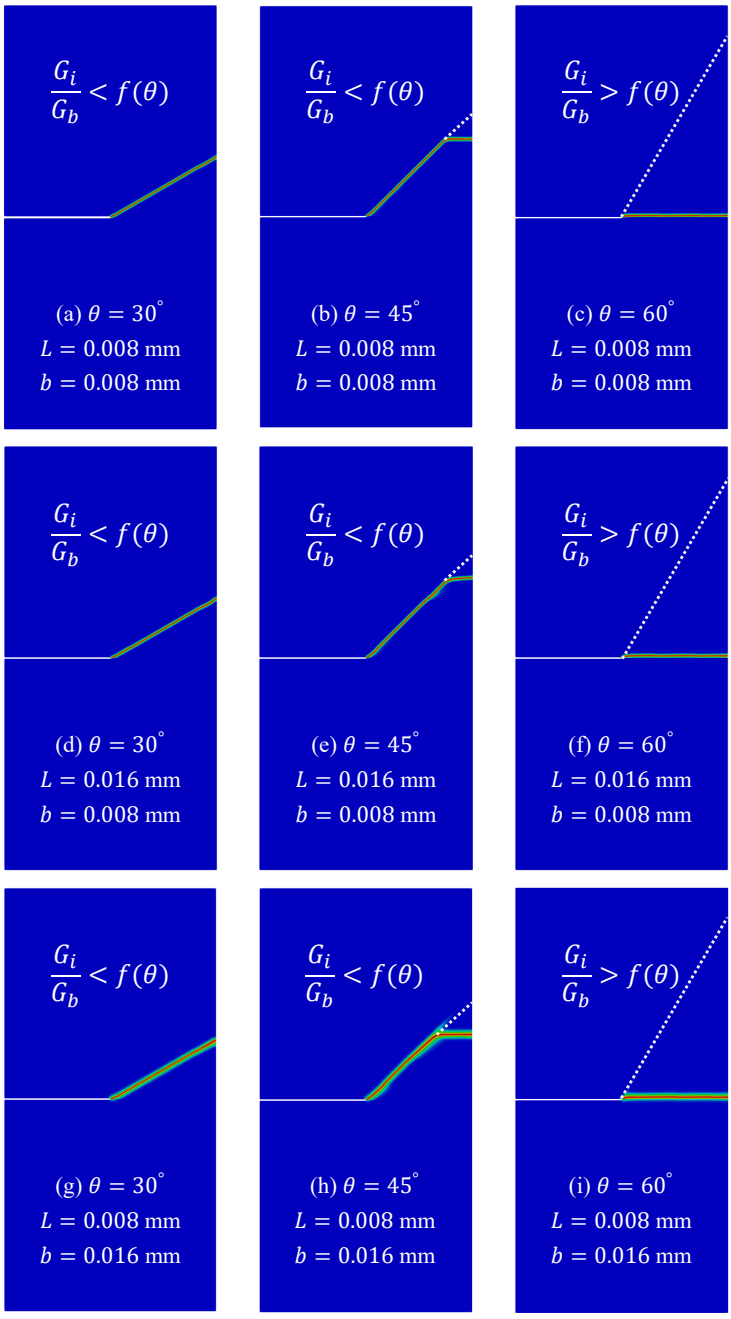

Figure 5: Crack phase-field results for a crack impinging on an interface under different interface inclined angle θ and length-scale parameters b, L. The crack deflects into the interface for the cases of $\theta = 30°$ (left column) and $\theta = 45°$ (middle column), while fracture penetrates into the bulk material for $\theta = 60°$ in the right column. Note the white dotted line indicates the interface.

$f(\theta = 60^\circ)$, the crack penetrates into the bulk. Above simulations based on the proposed model predict fracture modes at various inclined angles, which are consistent with the LEFM-based analytical criterion [91, 92]. Besides, for all aforementioned cases, different choices of length-scale parameters ($b\&L$) have negligible influences on the simulation results, except the width of diffusive damage zone. Moreover, quantitative results like structure reaction force predicted by the proposed model are also length-scale insensitive, details can refer to another purely-mechanical benchmark example in the Appendix C.

5.2. Chemo-mechanical benchmarks: Notched plates under de-lithiation

We are now looking into the chemo-mechanical case where the lithium flow drives the cracking progression in the charging (de-lithiation) process. The geometry adopted in the simulation is similar to the purely-mechanical case, specifically, a square-shape specimen consisting of 2-grains with connected grain boundaries (interface) and an introduced notch defect is considered. In the first subsection, we demonstrate the capability of the proposed model to accurately evaluate the competition between crack deflection and penetration in a chemo-mechanically coupled scenario. The second subsection presents simulations of inter-granular fracture, highlighting the model's length-scale insensitivity and its consistency with cohesive zone model predictions. Finally, the last subsection provides a benchmark example involving both inter-granular and trans-granular fractures.

Table 3: Material parameters in the chemo-mechanical examples taken from [24, 58, 62, 64, 81]

Material parameters	Value	Unit
Young's modulus E_0	93000	[GPa]
Poisson's ratio ν_0	0.3	[-]
Tensile strength of grain $\sigma_{c,b}$	600	[MPa]
Tensile strength of grain boundary $\sigma_{c,i}$	425	[MPa]
Fracture energy of grain G_b	5	[N/m]
Fracture energy of grain boundary G_i	4, 2.5	[N/m]
Maximum Lithium concentration $c_{\max}$	22900	[mol/m^3]
Partial molar volume Ω	3.497×10^{-6}	[m^3/mol]
Diffusivity D	7×10^{-15}	[m^2/s]
Gas constant R	8.314	[J/(mol·K)]
Temperature T	298.15	[K]

5.2.1. Crack impinging on an interface under chemo-mechanically coupled scenario

This example aims to study the competition between interface and bulk fracture modes under chemo-mechanical scenario. Similar to the setup of the purely-mechanical case, we consider a notched square plate of size 10 μm. As

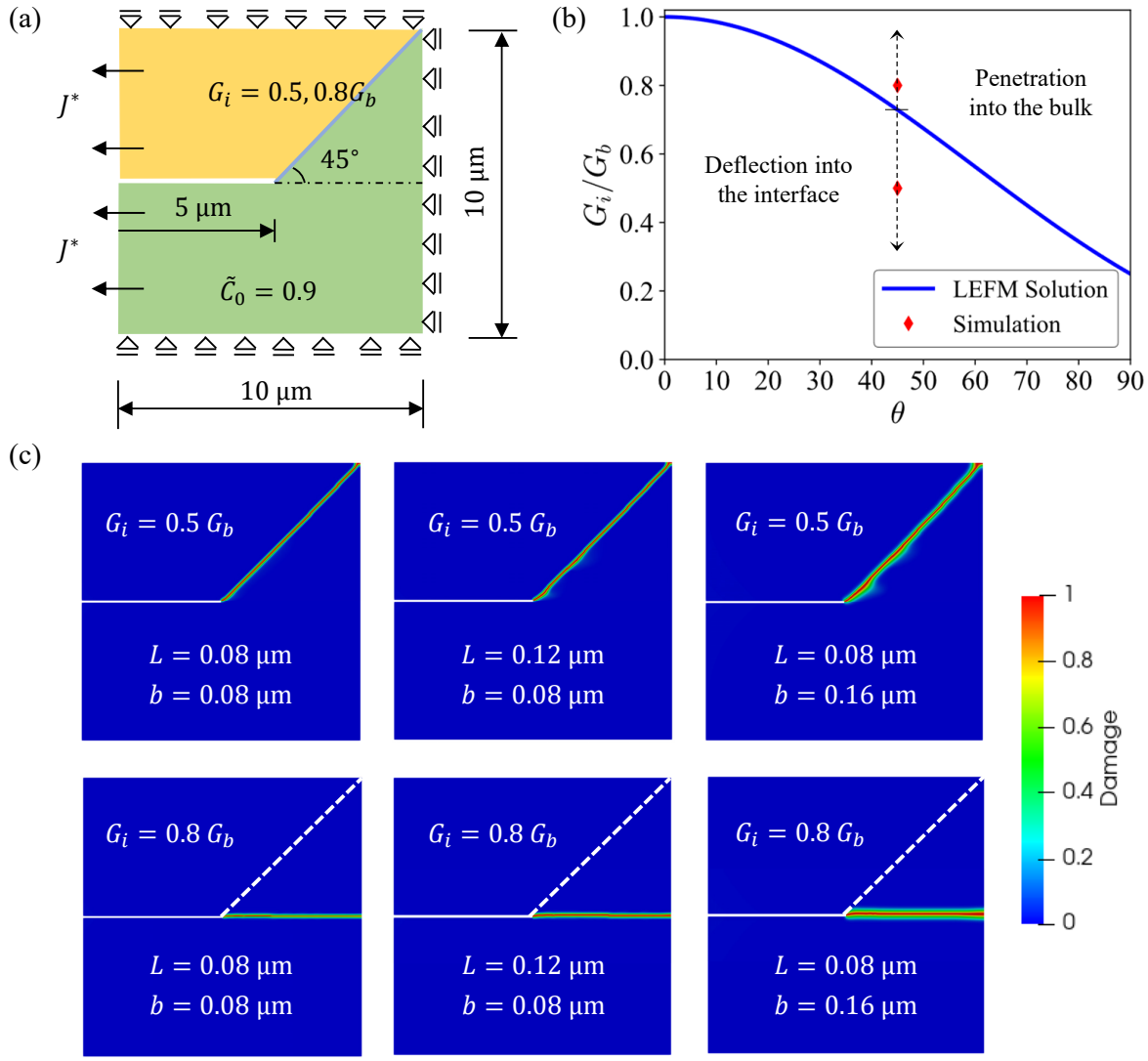

Figure 6: Crack impinging on an interface under chemo-mechanically coupled scenario. Figure (a) schematically illustrates the geometry, grain boundary, notch, mechanical and chemical boundary conditions. Figure (b) illustrates the predictions of deflection and penetration w.t.r. inclination angle (θ), which compares Linear Elastic Fracture Mechanics (LEFM) based analytical results [91, 92] and phase-field simulations from the proposed model. Figure (c) compares crack phase-field results obtained under varying interface fracture energy and length-scale parameters (b, L). Note the white dotted line indicates the interface.

shown in Figure 6 (a), a straight horizontal notch of half specimen's size at the middle height and an internal grain boundary of inclined angle $\theta = 45^\circ$ from the horizontal axis are introduced in the specimen. The whole system has initial concentration ($\tilde{c}_0 = c_0/c_{\max} = 0.9$) expressed in a normalized fashion and is assumed to be the stress-free initial state. Properly prescribed chemical and mechanical boundary conditions are considered, i.e., the de-lithiation flux is applied at the left edge and the displacement components along the normal directions of the left three edges are constrained. The parameters adopted in the simulation are listed in Table 3, in particular, we consider two different interface fracture energy, i.e., $G_i = 0.5, 0.8G_b$, anticipating distinct fracture modes to occur under aforementioned two cases, as illustrated in Figure 6 (b). In the simulation, the diffusivity (in Eq. (4.7c)) and partial molar volume (in Eq. (4.1b)) are assumed to be isotropic for simplicity. Besides, the influence of lengths-scale parameters ($b\&L$) are also studied through the simulations.

Figure 6 (c) compares the predicted crack phase-field results. As the lithium goes out from the left edge, the specimen undergoes volume shrinkage. Due to the mechanical boundary conditions on the other three edges constraining the deformation, tensile stress develops within the structure and crack nucleates at the tip of the notch. As can be noticed, for the case with high interface fracture energy, $\dfrac{G_i}{G_b} = 0.8 > f(\theta = 45^\circ)$ leads to the penetration of crack and the bulk failure mode; when it comes to the case with low interface fracture energy $\dfrac{G_i}{G_b} = 0.5$, crack deflects into the grain boundary with further propagation. Above simulation results agree with the analytical criterion [91, 92] on deflection (interface crack) vs. penetration (bulk crack) competition (see Figure 6 (b)), which also proves its potential applicability in multi-physical scenarios. Furthermore, the proposed cohesive phase-field model yields consistent crack patterns, regardless of the chosen phase-field or interface length-scale parameters ($b\&L$).

5.2.2. Simulation on chemo-mechanical inter-granular fracture

In this example, we focus on investigating the influences of length-scale parameters (b and L) in the proposed model on predicted chemo-mechanical inter-granular fracture results. As shown in Figure 7 (a), a similar specimen with a horizontal notch and a 30° slope grain boundary is considered. The material properties adopted in the simulations can refer to Table 3, here interface has relatively lower fracture energy $G_i = 0.5G_b$ than the bulk phase. A range of length-scale parameters (b and L) are considered in the simulations. The mechanical and chemical boundary conditions can refer to the setup in the previous example.

As the lithium flux goes out from the left edge, crack nucleates at the tip of the notch; subsequently, the crack propagates further along the weaker grain boundary till the specimen is completely divided into two separate parts. Figure 7 (b) compares the displacement profiles obtained by the CPF model and the CZM, after the complete propagation of inter-granular crack. Cohesive zone model and phase-field model give consistent predictions on specimen's global mechanical deformation, with observable displacement jumps at the grain boundary where fracture occurs. Figure 7 (c) and (d) compare predicted crack patterns under varied choices of parameters b and L. Despite different values of length-scale parameters adopted in the simulations, Model-S2 and Model-E2 yield consistent predictions of fracture patterns, by employing the precisely determined effective interface fracture energy so that the interface

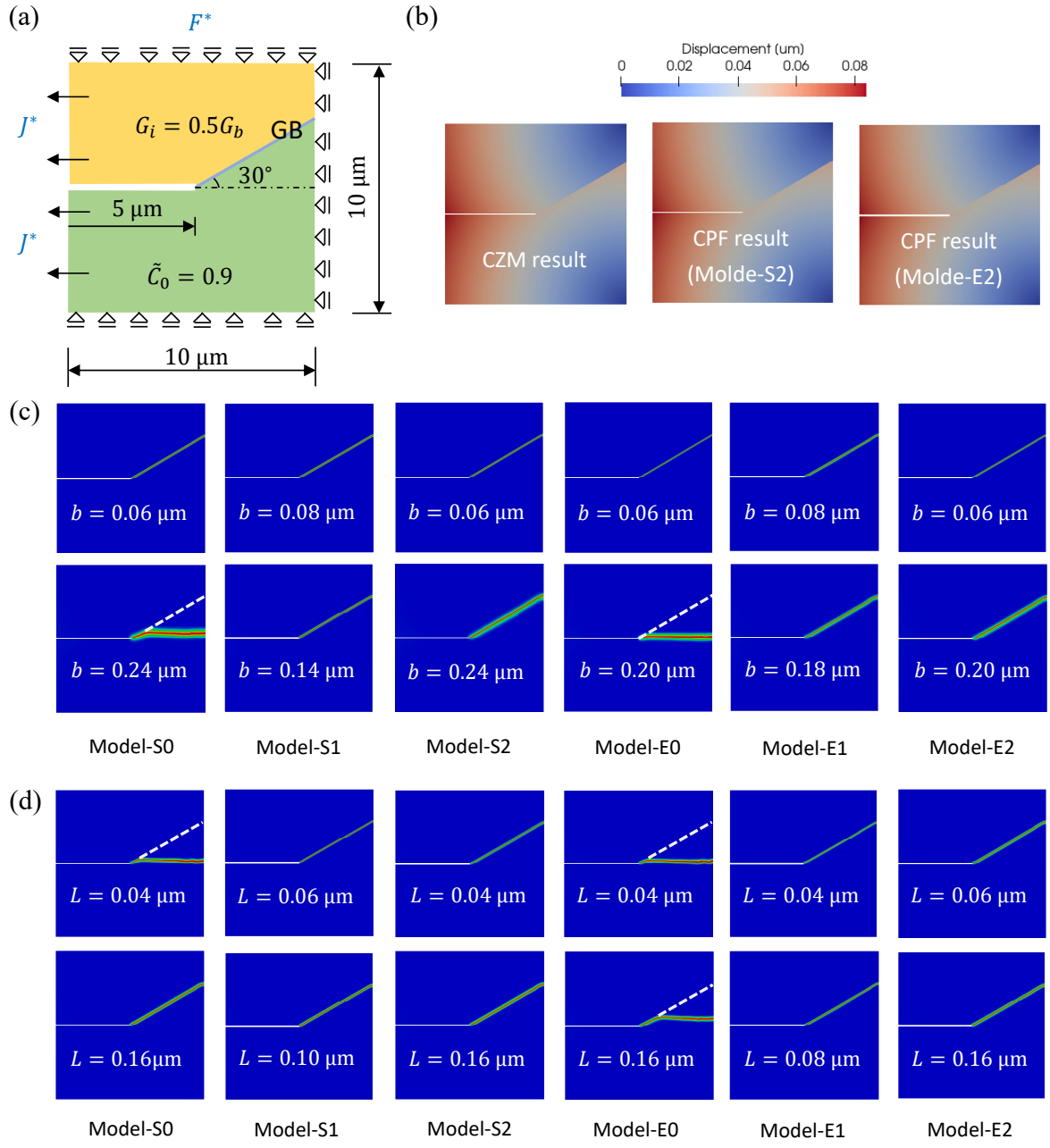

Figure 7: Single-edge notched plate with a 30-degrees slope GB under de-lithiation induced chemical flux. Figure (a) schematically illustrates the geometry, grain boundary, notch, mechanical and chemical boundary conditions. Figure (b) compares displacement results obtained by the CZM and the CPF model. Figure (c) and (d) compare crack phase-field results obtained by various CPF interface models under varying length-scale parameters b and L. Note the white dotted line indicates the interface/GB.

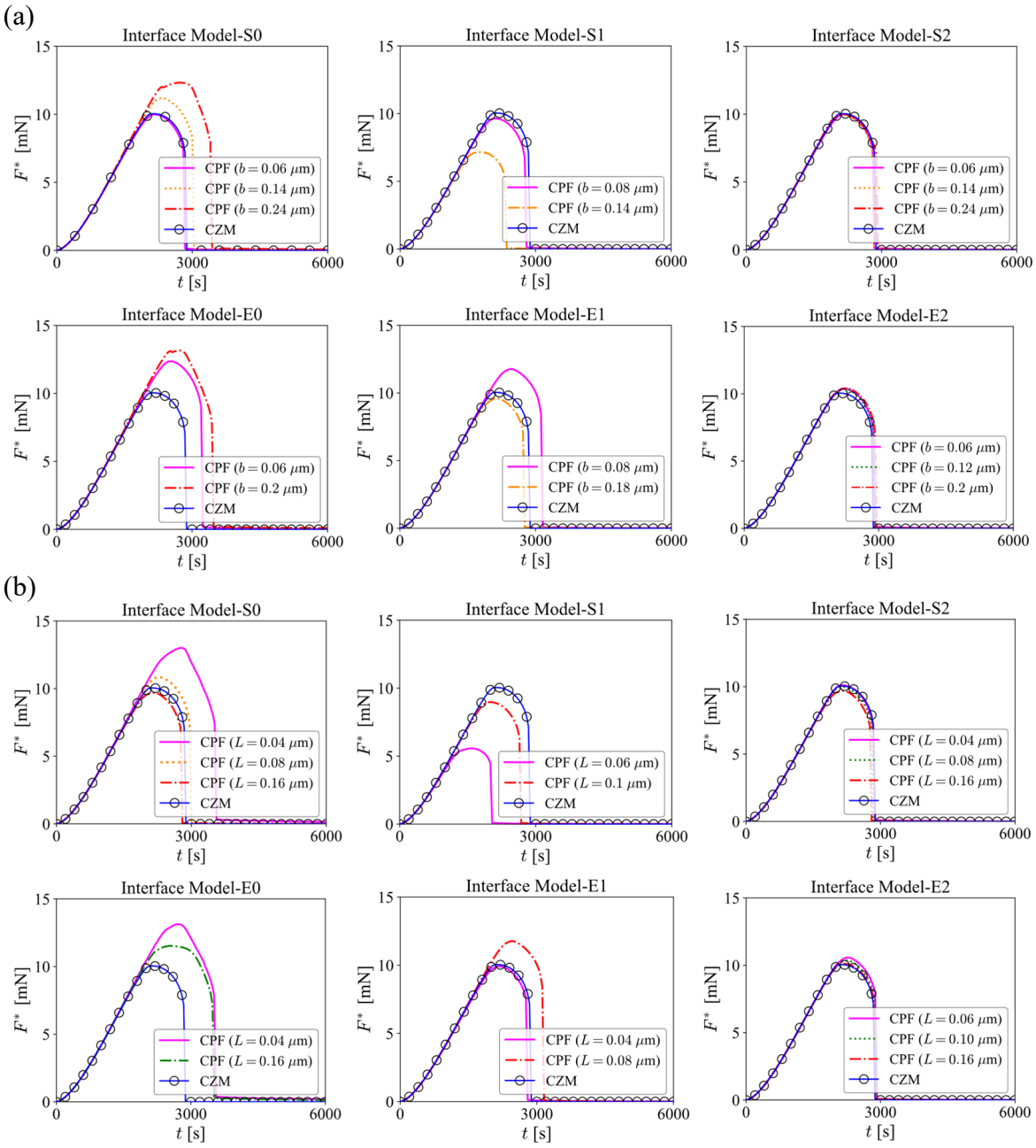

Figure 8: Figure (a) and (b) compare the structural reaction forces predicted by the CPF model and the CZM to study the influence of length-scale parameters b and L. Note for CPF simulations, a fixed value $L = 0.08$ μm is adopted for studying the influence of b, while $b = 0.12$ μm is fixed when investigating the effect of L.

fracture energy can be ensured to be equivalent to the sharp case. However, other interface models such as Model-S0 and Model-E0 obtain inconsistent predictions on failure patterns, which are length-scale sensitive/dependent. As can be seen, a larger b or a smaller L in those models tends to significantly overestimate the mechanical failure resistance of the interface, e.g., crack is observed to penetrate into the grain, which contradicts the criterion in Eq. (5.1) proposed by [91, 92], i.e., $\frac{G_i}{G_b} = 0.5 < f(\theta = 30^\circ)$ with interface delamination anticipated; while crack is predicted to propagate along the GB when b is smaller or L is larger.

Same conclusion can also be drawn from the comparison of quantitative structural reaction-force curves in Figure 8 (a) and (b). As can be seen, the overall global responses in Model-S2 and Model-E2, which agree well with predictions from the CZM, are negligibly affected by the choices of internal length-scale parameters b and L. In contrast, due to incorrect assess of fracture energy at the interface by Model-S0, Model-S1, Model-E0 and Model-E1, unconvincing results are obtained, which show strong dependency/sensitivity on the choices of length-scale parameters.

5.2.3. Simulation on chemo-mechanical inter- and trans-granular fractures

In this subsection, we employ the proposed chemo-mechanical CPF model to analyze an example encompassing both inter- and trans-granular fractures. This serves the purpose of simulating potential crack paths in polycrystalline cathodes, which possibly start in the grain and then evolve towards grain boundaries. As shown in Figure 9 (a), two individual grains are connected with the grain boundary. One horizontal notch with quarter length of the specimen is introduced in the left grain, so that trans-granular crack could nucleate here. The simulation setups, e.g., materials properties, initial and boundary conditions, can refer to the previous example. Given the limitations of the CZM in modeling bulk fracture or trans-granular cracking behaviors [10], in this example, only phase-field modeling is considered, specifically, Model-S2 and Model-E2 are adopted in the simulations to validate their respective performances.

Figure 9 (b) compares the fracture patterns obtained with Model-S2 and Model-E2. As the lithium flux goes out from the left edge, chemical deformation leads to local high mechanical stress and crack nucleation at the notch tip. Over time and as delithiation progresses, the fracture firstly propagates within the left grain and subsequently deflects towards the GB with relatively weaker failure resistance, leading to intricate inter- and trans-granular failure modes. As can be seen, identical crack patterns are obtained in the simulations in spite of varied choices of length-scale parameters b and L, which only affects the width of the diffusive phase-field damage band. Regardless of stair-wise (in Model-S2) or exponential (in Model-E2) representation of interface in the modeling, the approach ensuring interface fracture energy consistent with that in the cohesive zone model is very robust in chemo-mechanical phase-field fracture simulations, which gives length-scale insensitive numerical predictions.

Furthermore, Figure 9 (c) compares reaction force w.r.t. delithiation time obtained with Model-S2 and Model-E2. As can be concluded, internal length-scale parameters b and L have negligible effects on global structural responses, which applies to both stair-wise (Model-S2) and exponential (Model-E2) interpolations of fracture energy.

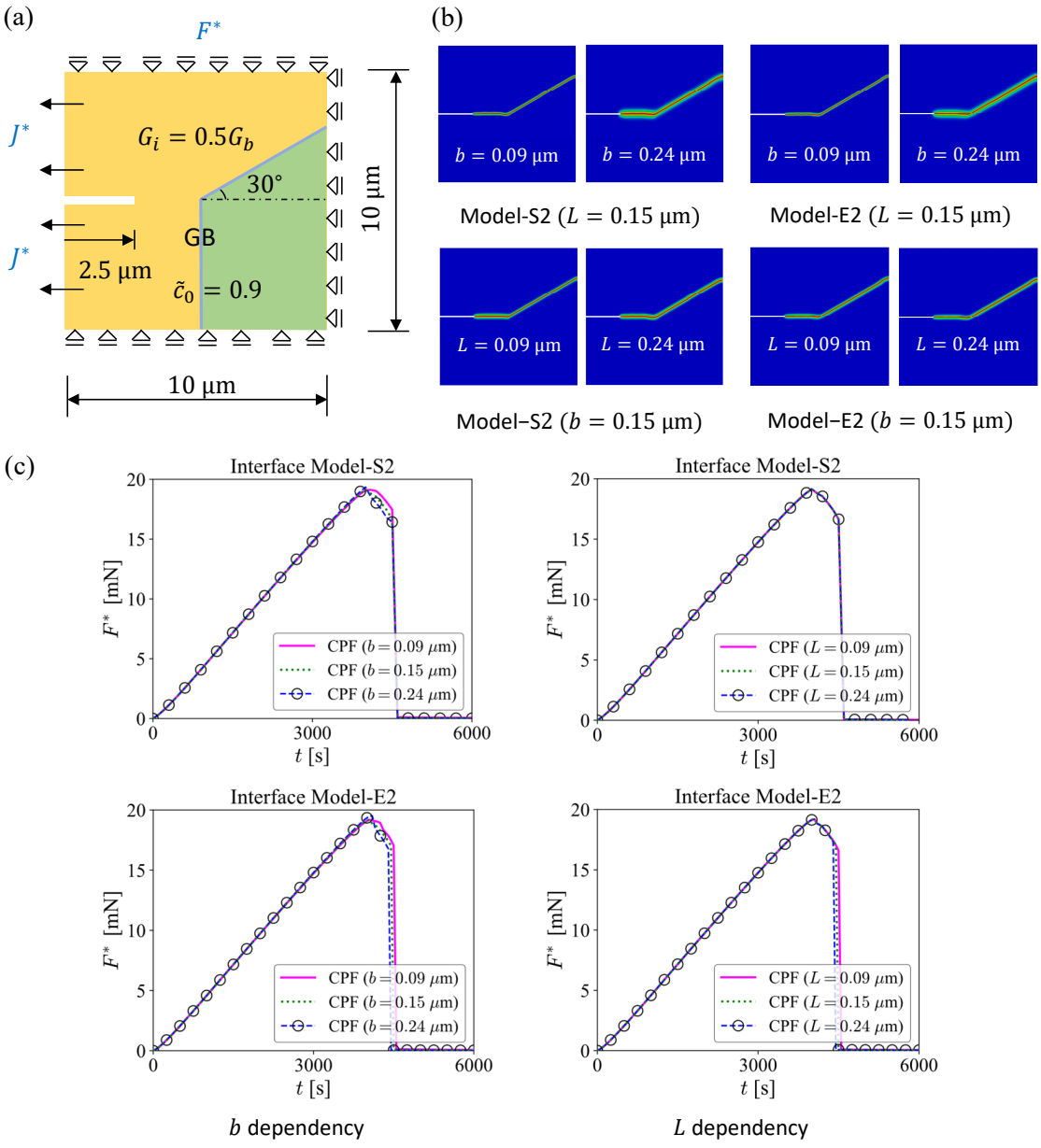

Figure 9: Single-edge notched plate with grain boundary and notch under de-lithiation induced chemical flux and proper mechanical constraints. Figure (a) schematically illustrates the geometry, grain boundary, mechanical and chemical boundary conditions. Figure (b) compares the phase-field crack results obtained by CPF Interface Model-S2 and Model-E2 with varying length-scale parameters b and L. Figure (c) shows the structural reaction forces for illustrating the independence of obtained results on length-scale parameters b and L.

5.3. Chemo-mechanical application: Image-based reconstructed 3D NMC cathode geometry

In the present section, the proposed chemo-mechanical phase-field model is applied to image-based reconstructed 3D NMC cathode particles, see Figure 11 (a) and (b) for the visualization of the geometry. In addition to ensuring consistency of interface fracture energy with the cohesive zone model and providing length-scale insensitive predictions, the proposed new Model-E2 is particularly notable for its flexibility in handling intricate grain boundaries/interface topologies within 3D polycrystalline microstructures, which will be highlighted in this example.

The generation and meshing of cathode polycrystalline geometry are briefly reviewed, readers can refer to [31, 93] for further details on this process. Statistical characterizations of the outer shell of $Li_xNi_{0.5}Mn_{0.3}Co_{0.2}O_2$ (NMC532) particles are obtained from nano-computed tomography (nano-CT) data, while grain architectures are determined from focused-ion beam (FIB) and electron backscatter diffraction (EBSD) data, integrated within a 3D stochastic model. A resource for above scanning data of battery electrode architectures is the NREL Battery Microstructure Library, see `https://www.nrel.gov/transportation/microstructure.html`. Subsequently, two models are combined to generate virtual NMC particles together with their inner grain architectures, which possess statistically similarities to those observed in the nano-CT and FIB-EBSD data [93]. In phase-field simulations, a subset of 8 and 69 grains composing the secondary particle with a volume of 370 μm^3 are extracted from the full-grain architecture [81], which are eventually processed with `Iso2Mesh` (an open-source MATLAB code that converts images into meshes [94]) for finite-element mesh generations, as visualized in Figure 11 (a) and (b).

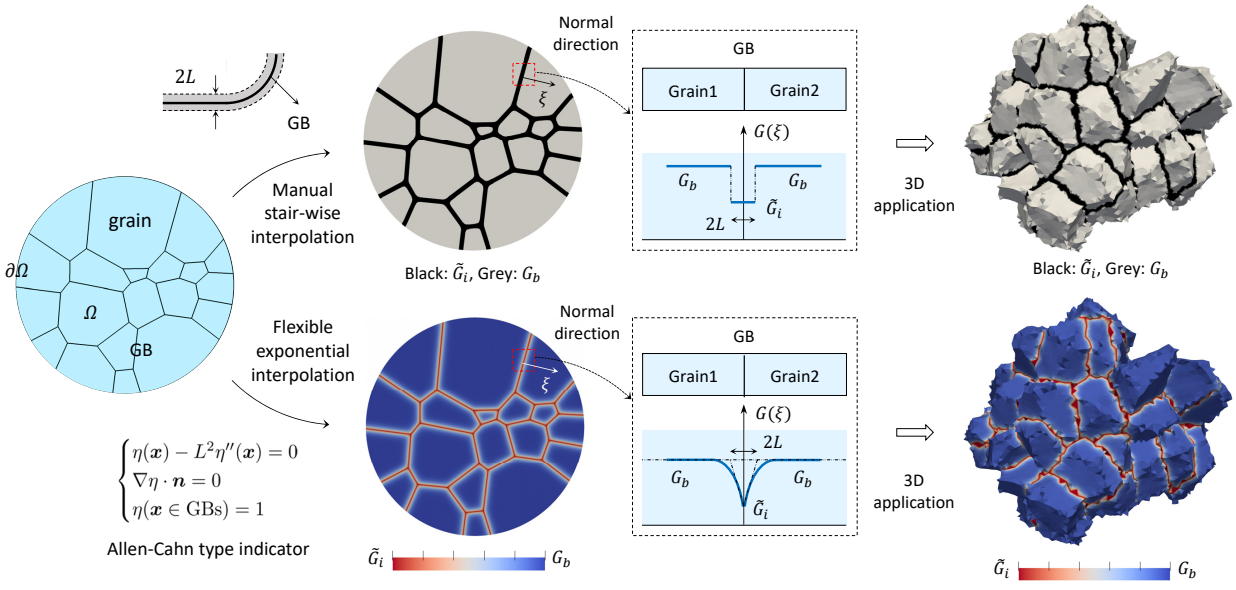

Figure 10: Comparison of implementations of stair-wise (in Model-S2) and exponential (in Model-E2) functions for the interpolation of fracture energy between the grains and the GBs in a polycrystalline microstructure.

To assign the fracture energy $G(\boldsymbol{x})$ within the polycrystalline domain for simulations, implementations of stair-wise and exponential functions for interpolating the fracture energy between the grains and the grain boundaries are

illustrated in Figure 10. As for Model-S2, a diffusive interface region with a width of $2L$ in the normal direction of the GBs needs to be manually generated, where the effective interface fracture energy $\tilde{G}_i$ is assigned; while the left regions possess the bulk fracture property G_b, so that stair-wise distribution $G(\xi)$ at the GBs' normal direction can be observed in the zoomed call-out. However, when dealing with a 3D polycrystalline structure with complex interface topologies, manually selecting the material points within the $2L$-wide diffusive interface region becomes increasingly cumbersome to implement. Instead, Model-E2 employs an Allen-Cahn type GBs (interface) indicator $\eta(\boldsymbol{x})$ to achieve the exponential interpolation of fracture energy between GBs and grains as Eq. (3.15) shows. This approach offers greater flexibility in handling intricate GB topologies, as demonstrated in 2D and 3D polycrystalline microstructure, it allows a smooth transition of fracture property, eliminating the need to manually define the diffusive GB region with a prescribed width, as required in Model-S2.

In the modeling, material properties can refer to Table 3 of the previous example. In order to consider anisotropic behaviors in reconstructed 3D particles, a transversely isotropic model [81, 83] distinguishing properties between the directions of in-plane (a-b) and out-of-plane (c) is considered, see Figure 11 (a) for an illustration; specifically, for the diffusivity tensor and partial molar volume tensor,

$$\boldsymbol{D} = \boldsymbol{R}\begin{bmatrix} D_{ab} & 0 & 0 \\ 0 & D_{ab} & 0 \\ 0 & 0 & D_c \end{bmatrix}\boldsymbol{R}^{\mathrm{T}}, \qquad \boldsymbol{\Omega} = \boldsymbol{R}\begin{bmatrix} \Omega_{ab} & 0 & 0 \\ 0 & \Omega_{ab} & 0 \\ 0 & 0 & \Omega_c \end{bmatrix}\boldsymbol{R}^{\mathrm{T}}, \tag{5.2}$$

here $\boldsymbol{R}$ denotes the rotation matrix determined from the crystal orientation of the grain. According to literature [55, 81, 95–97], the in-plane diffusion coefficient is typically assumed to be 100 times faster as compared to the out-of-plane one, i.e., $D_{ab} = 100D_c = D$; similarly, the partial molar volume is assumed to be 5 times larger in the out-of-plane direction as compared to the in-plane, namely, $\Omega_{ab} = 5\Omega_c = \Omega$. It has been observed from several previous benchmarks that the length-scale parameters have negligible influence on numerical predictions, such as crack evolution paths and quantitative global responses. Therefore, for the simulations in this subsection, we consider $b = 0.4$ μm and $L = 0.2$ μm.

Regarding the boundary conditions, rigid-motion suppression is specified by fully constraining translation on one central point and partially constraining rotation on two points on the outside surface [31, 81]. The electrostatic and electrochemical potential at the interface between the active material and the electrolyte determines how chemical reaction ($\mathrm{Li}^+ + e^- \rightleftharpoons \mathrm{Li}$) takes place and the lithium flux on the secondary-particle surface, which can be described by the modified Butler–Volmer (BV) equation [24, 58, 68],

$$J^* = \frac{c_{\mathrm{surf}}}{\tau_0}(1-\tilde{c})\left[\exp\left(-\frac{F}{2RT}\Delta\phi\right) - \exp\left(\frac{\mu}{RT} + \frac{F}{2RT}\Delta\phi\right)\right], \tag{5.3}$$

where c_{surf} is the molar concentration of intercalation sites on the surface, τ_0 denotes the mean duration for a single reaction step which accounts for the slow and fast reaction, F is Faraday's constant, $\Delta\phi = \phi_{\mathrm{e}} - \phi(\tilde{c})$ is the voltage difference across the interface (refer to [81, 98] for detailed information) and μ expressed in Eq. (4.7b) is the chemical

potential at the interface between active material and the electrolyte. For the given 10C-rate used in the simulation, one circle with initially discharging (lithiation) from SOC = 0.3 to 0.9 and subsequently charging (de-lithiation) till SOC = 0.3 is adopted as chemical boundary condition to simulate charging/discharging scheme.

The influence of sharp interface fracture energy on crack patterns is firstly studied. Figure 11 (d) illustrates the concentration and crack phase-field results, under the assumption that grain boundaries and grains have identical fracture energy ($G_i = G_b$). As can be seen, during the first half stage with increasing lithium concentration and SOC (state of charging, to denote the average Li concentration in units of $c_{\max}$), lithium insertion induces volume expansion and correspondingly mechanical stress leads to crack nucleation and evolution from the interior of the structure to the exterior, which agrees with previous simulations [31, 101]. During de-lithiation, as the lithium concentration decreases, tensile stress develops at the hoop/tangential directions of the particle's exterior part [24, 56] due to global volume shrinkage. This stress leads to further propagation of cracks from the exterior [31, 48], eventually merging with the previously formed cracks [102] and splitting the grains. Besides, intricate patterns such as branching and merging of cracks can be simulated by phase-field model under given fast charging scheme, as did in previous simulations [70, 101]. For the case when grain boundaries have lower fracture energy than the grains [7, 43], e.g., $G_i = 0.5G_b$ is assumed in the simulation, as shown in Figure 11 (e), during the lithiation stage, cracks tend to emerge and grow at the GBs with lower fracture energy [24, 25], so that an inter-granular failure mode can be observed; under de-lithiation condition, trans-granular fractures (see Figure 11 (c) for experimentally obtained cracks and others [46, 47]) occur within the grains and merge with the inter-granular ones, with some exhibiting branching patterns. As can be concluded, interface fracture energy plays an important role in determining the failure modes of the polycrystalline cathode particle.

Subsequently, the influence of grain size on fracture behaviors of polycrystalline cathode particles is investigated with the proposed model. Figure 11 (f) illustrates the crack phase-field results of a reconstructed 3D cathode particle, which has the same volume as the 8-grains particle but contains more (69) smaller grains. During the lithiation stage, cracks nucleate from the interior and evolve to the exterior, which behaves similarly to the 8-grains particle; after switching to de-lithiation condition, more cracks appear in the structure merging together with each other, leading to global degradation of the cathode particle. The obtained fracture patterns are dominantly inter-granular cracks, which presents the agreement with experimentally observed cracks in Figure 11 (c) and previous simulations on the cathode particle [24, 25] and similar polycrystalline structures [19, 85]. Comparing the fracture behaviors of particles with the same volume but different grain size, it can be concluded that, inter-granular cracks at the GBs predominantly dictate the failure mode when grain size is smaller, while both inter- and trans-granular patterns can happen when grain size is larger, which agrees with the findings in previous studies [24, 31].

Eventually, it should be pointed out, numerical predictions on chemo-mechanical fracture, obtained by the proposed new phase-field interface Model-E2 with exponential interpolation of fracture energy, align with those based on the Model-S2 with stair-wise interpolation. This agreement is attributed to the achieved consistency between the phase-field integrated interface fracture energy and the sharp value defined in the classical cohesive zone model,

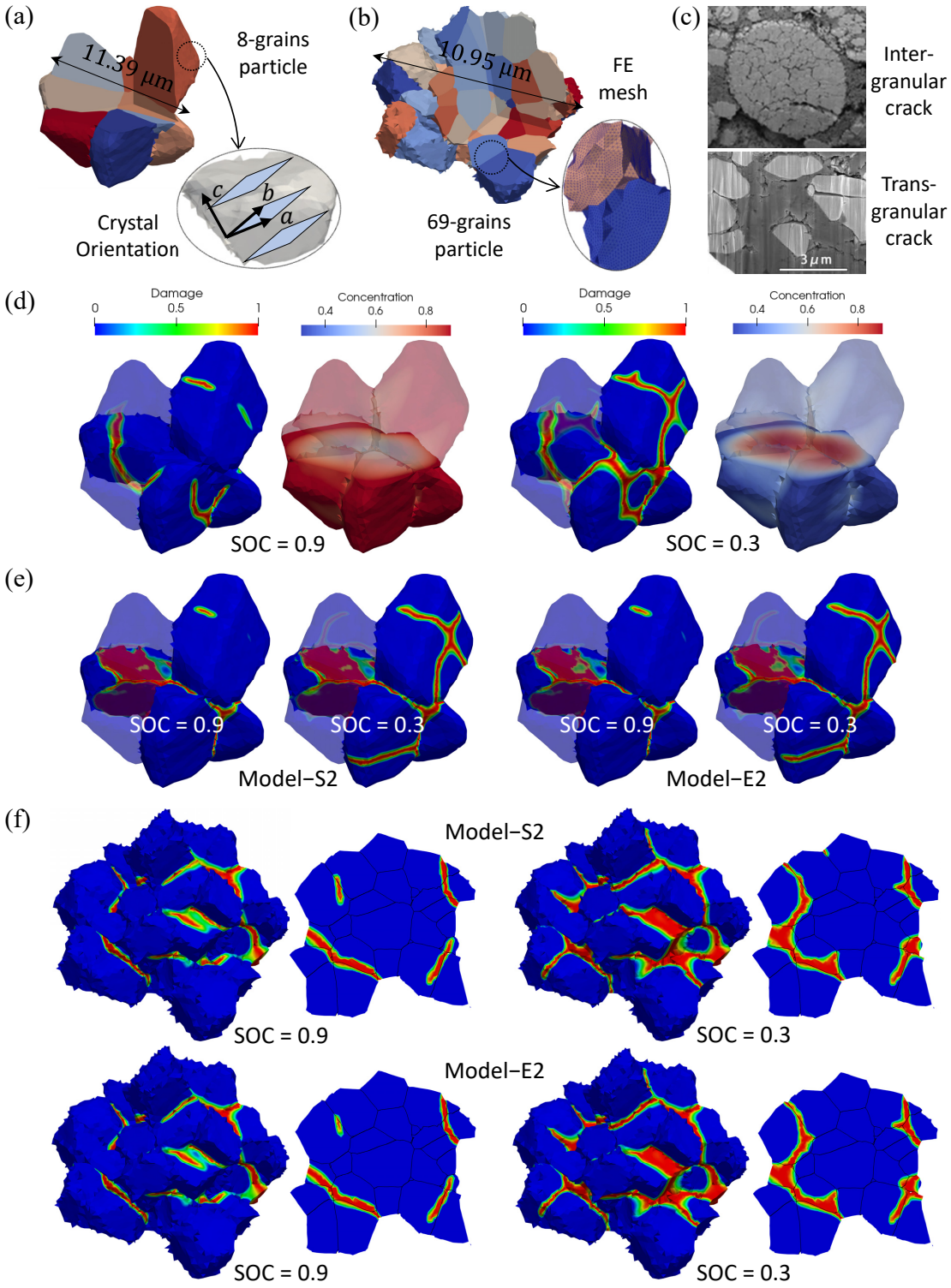

Figure 11: Chemo-mechanical simulation results on image-based reconstructed 3D NMC cathode particles. Figure (a) and (b) show the geometry and polycrystalline microstructure of two particles consisting of 8 and 69 grains, respectively; finite-element meshes and crystal orientations for transversely isotropic model are also illustrated. Figure (c) shows the experimentally observed inter-granular [99] and trans-granular [100] fracture patterns in a NMC polycrystalline particle. Figure (d) shows the concentration and crack phase-field results at the ending moments of lithiation (SOC=0.9) and de-lithiation (SOC=0.3), respectively. Figure (e) and (f) compare the fracture patterns of particles comprising of 8 and 69 grains, respectively, which are obtained by two interface models (Model-S2 and Model-E2). For the 69-grains particle case, fracture results within a section are also depicted.

which applies to concurrent bulk and interface fracture, as seen in Eq. (3.16). However, based on the aforementioned simulations of image-based 3D reconstructed polycrystalline cathode particles, the proposed CPF interface model with exponential interpolation of fracture property exhibits advantages over other models due to its high flexibility in handling structures containing complicated GBs topology, which is achieved through the auxiliary indicator variable solved from the Allen-Cahn equation.

6. Conclusions

In this study, we proposed a new cohesive phase-field interface fracture model, the new model is on the basis of Euler-Lagrange equation of the variational problem and interface fracture energy check w.r.t that of the cohesive zone model. It utilizes an exponential function, which is constructed conveniently with the Allen-Cahn type auxiliary indicator, for the interpolation of fracture energy between the bulk phase and the interface within the structures consisting of complicated GBs topology; while the effective interface fracture energy $\tilde{G}_i$ is derived in such a way that the integrated phase-field fracture energy across the diffusive interface region remains consistent to that of the sharp interface fracture energy G_i defined in the classical cohesive zone model.

The proposed phase-field interface model is further extended to multi-dimensional formulation and seamlessly integrated into the chemo-mechanically coupled scenario in a thermodynamically consistent manner for the Lithium-ion battery cathode materials. The above multi-physically coupled cohesive phase-field fracture model is numerically implemented with finite-element method in an open-sourced platform MOOSE.

Benchmark examples of square plates with predefined notch and internal interface/grain boundary under both mechanical and chemo-mechanical scenarios highlight following merits of the proposed model. Concurrent bulk (trans-granular) and interface (inter-granular) fracture behaviors can be simulated with the proposed unified model. Examples of crack impinging on an interface regarding the competition between bulk and interface fractures are presented, which agree with the LEFM-based analytical results. Thanks to the constructed consistency between the integrated phase-field interface fracture energy and the sharp value defined in the cohesive zone model, numerical outcomes like crack evolution pattern, displacement and structural reaction force given by the proposed model consistently align with predictions from the CZM. In addition, numerical results demonstrate insensitivity/independence with respect to length-scale parameters, i.e., the regularized thicknesses of phase-field fracture surface b and interface L.

Eventually, the coupled CPF model is applied to chemo-mechanical simulations of image-based reconstructed 3D NMC polycrystalline particles, which validates the high flexibility offered by our proposed phase-field interface Model-E2 in handling 3D polycrystalline structure with complicated GBs topology. The influences of sharp interface fracture energy and grain size on chemo-mechanical fracture behaviors are studied and validated with previously published experiment and simulation results. It can be concluded from numerical simulations, the fracture energy of the GBs significantly affect the fracture modes in NMC polycrystalline particles; besides, particles with large grain

size can yield both inter- and trans-granular cracks, while inter-granular fracture mode is dominantly exhibited for particles with small grain size.

Looking forward, our outlooks encompass two potential areas for future investigation. Firstly, as mentioned in the Section 4, the anisotropic properties of the polycrystalline microstructure including the elastic stiffness and fracture energy can be considered as grain-orientation-dependent, like in [19, 85]. Secondly, the effect of electrolyte and its coupling with fracture propagation is ignored in the current manuscript. Depending on the (liquid/solid) state of employed electrolyte, the impacts of cracks on the chemical process can vary, e.g., cracks lead to an increase in electrochemically active surface areas and an improvement in charge-transfer kinetics due to the wetting effect [103] in liquid electrolytes, while interface separation at electrode/solid electrolyte degrades and impede the kinetics [104, 105]. Such influence will be further incorporated into the current framework in our future studies.

Acknowledgments

The authors Chen and Xu gratefully acknowledge the computing time granted on the Hessian High-Performance Computer "Lichtenberg" (Project-02017, Special-00007). This work has been (partially) funded by the German Research Foundation (DFG) under grant 460684687. The third author Wu acknowledges the support from the National Natural Science Foundation of China (52125801). The authors would like to express deep gratitude to Dr. Jeffery M. Allen and Prof. Dr. Kandler Smith in National Renewable Energy Laboratory, Golden, USA, for their help with the generation of finite-element mesh of image-based reconstructed 3D NMC polycrystalline particles.

Appendix A. The effective interface fracture energy defined in Model-S0, Model-S1 and Model-S2

Aforementioned three models all adopted the stair-wise interpolation function $A(x) = H(x)$ in Eq. (3.1), so that fracture energy in the diffusive interface region $x \in [-L, L]$ is a constant. Model-S0 [31, 74, 75] directly assigns the property with the sharp value G_i, so that the resulted phase-field profile $d(x)$ is supposed to be obtained by solving the Euler-Lagrange equation expressed in Eq. (3.5),

$$d(x) = \begin{cases} 1 - \epsilon \sin\left(\dfrac{|x|}{b}\right), & \text{when } |x| \le L \\ 1 - \sin\left(\dfrac{|x|}{b} + \theta\right), & \text{when } L < |x| \le \left(\dfrac{\pi}{2} - \theta\right) b \\ 0, & \text{else} \end{cases}, \quad \text{with} \quad \begin{cases} \epsilon = 1 / \sqrt{\sin^2\left(\dfrac{L}{b}\right) + \left(\dfrac{G_i}{G_b}\right)^2 \cdot \cos^2\left(\dfrac{L}{b}\right)} \\ \theta = \tan^{-1}\left[\dfrac{G_b}{G_i} \tan\left(\dfrac{L}{b}\right)\right] - \dfrac{L}{b} \end{cases}, \tag{A.1}$$

which is visualized in Figure 1 (b). For the analytical derivation process for the solution $d(x)$ under stair-wise $G(x)$, interested readers are suggested to refer to [29, 76]. By substituting above phase-field profile $d(x)$ for integration, we can get the results in Eq. (3.6) to analyze the model's consistency with the sharp interface fracture energy and the corresponding issue of length-scale sensitivity.

In the Model-S1 [27, 28], an effective interface fracture energy is proposed to constrain the integrated phase-field fracture energy to be consistent with the sharp property, e.g., for the energy constraint equation,

$$\int_{-\infty}^{+\infty} \psi_d(x, d, d')\, \mathrm{d}x = G_i, \tag{A.2}$$

the phase-field profile $d(x)$ in Eq. (2.5) for homogeneous material with spatially uniform fracture energy is substituted into above equation, and one can obtain following expression of $\tilde{G}_i$,

$$\tilde{G}_i = \left[G_i - (1 - B) G_b\right] / B, \quad \text{with} \quad B = 2 \int_0^L \gamma\left(d, d'\right) \mathrm{d}x = \frac{1}{\pi}\left[\frac{2L}{b} + \sin\left(\frac{2L}{b}\right)\right]. \tag{A.3}$$

Above result of $\tilde{G}_i$ w.r.t. L/b is visualized in Figure 1 (i). However, for a heterogeneous material system including both bulk and diffusive interface, it is not appropriate to assume the phase-field profile within Eq. (A.2) identical to that under spatially uniform fracture property. Accepting above defined $\tilde{G}_i$ in the Model-S1, the phase-field profile $d(x)$ is supposed to be obtained by solving the Euler-Lagrange equation, which is in a similar fashion to Model-S0

and its result is visualized in Figure 1 (c). Same procedure of substituting obtained profile result into the integration is repeated to get the expression in Eq. (3.7).

In the Model-S2 [29, 76], the phase-field profile $d(x)$ in the energy constraint equation Eq. (A.2) is solved from the Euler-Lagrange equation and expressed w.r.t. the unknown effective interface fracture energy $\tilde{G}_i$ as following,

$$d(x) = \begin{cases} 1 - \tilde{\epsilon}\sin\left(\dfrac{|x|}{b}\right), & \text{when } |x| \le L \\ 1 - \sin\left(\dfrac{|x|}{b} + \tilde{\theta}\right), & \text{when } L < |x| \le \left(\dfrac{\pi}{2} - \tilde{\theta}\right) b \\ 0, & \text{else} \end{cases}, \quad \text{with} \quad \begin{cases} \tilde{\epsilon} = 1/\sqrt{\sin^2\left(\dfrac{L}{b}\right) + \left(\dfrac{\tilde{G}_i}{G_b}\right)^2 \cdot \cos^2\left(\dfrac{L}{b}\right)} \\ \tilde{\theta} = \tan^{-1}\left[\dfrac{G_b}{\tilde{G}_i}\tan\left(\dfrac{L}{b}\right)\right] - \dfrac{L}{b} \end{cases}. \tag{A.4}$$

With above explicitly expressed profile result, constraining equation that ensures the integrated phase-field fracture energy equivalent to that of sharp interface can be further simplified so that $\tilde{G}_i$ can be solved, namely,

$$\int_{-\infty}^{+\infty} \psi_d(x, d, d')\,\mathrm{d}x = G_i \qquad \Longrightarrow \qquad \frac{L}{b}\frac{\tilde{G}_i}{G_b} - \tan^{-1}\left[\frac{G_b \tan\left(\frac{L}{b}\right)}{\tilde{G}_i}\right] + \frac{\pi}{2}\left(1 - \frac{G_i}{G_b}\right) = 0. \tag{A.5}$$

A visualization of obtained $\tilde{G}_i$ from above equation in terms of given length-scale parameters b and L can be seen in Figure 1 (i) under the condition $G_i = 0.5G_b$. Figure 1 (d) depicts the phase-field profile $d(x)$ in Eq. (A.4) under stair-wise $G(x)$ with solved $\tilde{G}_i$. In the Model-S2, the interface fracture energy within the phase-field framework is consistent with that defined in the sharp approach, as shown in Eq. (3.8).

Appendix B. Formulations of cohesive zone model for chemo-mechanical fracture

In this section, the chemo-mechanical cohesive zone model for simulating fracture in Lithium-ion batteries is briefly recalled. The governing equations and corresponding constitutive laws of the bulk (Ω) for chemical and mechanical sub-problems are listed as following.

$$\begin{cases} \nabla \cdot \boldsymbol{J} + \dot{c} = 0 \\ \mu = RT \ln \dfrac{\tilde{c}}{1 - \tilde{c}} - \boldsymbol{\sigma} : \boldsymbol{\Omega} \\ \boldsymbol{J} = -c(1 - \tilde{c})/(RT)\boldsymbol{D} \cdot \nabla\mu \end{cases} \tag{B.1a}$$

$$\begin{cases} \nabla \cdot \boldsymbol{\sigma} = \boldsymbol{0} \\ \boldsymbol{\sigma} = \mathbb{E}_0 : (\boldsymbol{\epsilon} - \boldsymbol{\epsilon}_c) \end{cases} \tag{B.1b}$$

With particular interest and focus on fracture behaviors, here the diffusion across the GB/interface (Γ) is assumed to be coherent and continuous for simplicity, while the crack evolution on the interface is captured with cohesive zone model as following,

$$\int_\Gamma (\boldsymbol{t}^+ \cdot \delta\boldsymbol{u}^+ + \boldsymbol{t}^- \cdot \delta\boldsymbol{u}^-)\,\mathrm{d}A = \int_\Gamma \boldsymbol{t} \cdot \delta[\![\boldsymbol{u}]\!]\,\mathrm{d}A \tag{B.2}$$

which can be obtained by applying divergence theorem to strong form in Eq. (B.1), here $\boldsymbol{t}^{+} = -\boldsymbol{t}^{-} = \boldsymbol{t}$ satisfies the mechanical equilibrium at the interface, and $\boldsymbol{t}$ denotes the traction force. In the CZM, the displacement jump is adopted to characterize the fracture evolution, i.e., total jump in global coordinate system is expressed as $[\![\boldsymbol{u}]\!] = \boldsymbol{u}^{+} - \boldsymbol{u}^{-}$, so that the jump in interface coordinate system $[\![\tilde{\boldsymbol{u}}]\!] = \tilde{\boldsymbol{R}}[\![\boldsymbol{u}]\!]$ can be obtained with rotation matrix $\tilde{\boldsymbol{R}}$.

The local traction force at the interface $\tilde{\boldsymbol{t}}$ can be determined from the cohesive zone constitutive model, i.e., traction-separation law (TSL), w.r.t. to the local displacement jump $[\![\tilde{\boldsymbol{u}}]\!]$, then traction force in global coordinate system $\boldsymbol{t}$ (Eq. (B.2)) can be obtained. In the modeling, bilinear softening law [106] is adopted to characterize tension-dominant fracture behaviors. For further details, readers are referred to [58, 64], including more complicated contexts such as mixed-modes fracture and large mechanical deformation setup.

Appendix C. Purely-mechanical benchmark: Notched plate under tensile loading

The merits of the proposed model, including length-scale insensitivity and consistence with the cohesive zone model's predictions, are verified in this purely-mechanical example. As shown in Figure C.12 (a), it is a square plate of length 1 mm, with unit out-of-plane thickness. A straight horizontal notch, measuring 0.5 mm in length, is introduced at the half height of the specimen; and a horizontal internal interface connects between the right end of the notch and the midpoint of specimen's right edge, bridging the upper and lower parts. The bottom edge is fixed, while a vertical displacement is applied on the top edge.

The purely-mechanical CPF model can be obtained by switching off the chemical process in the fully coupled model in Section 4. The corresponding material parameters adopted in the simulations are listed in Table 2, here the interface possesses relatively weaker strength and fracture energy than the bulk phase. In order to study the influences of length-scale parameters on numerical results, parametric studies with diverse values of b and L within different interface models are investigated. Besides, for numerical simulations conducted with the cohesive zone model, identical values in Table 2 are used, except two length-scale parameters which are not involved in the CZM.

Along with increasing mechanical loading, the crack initially originates at the tip of the notch due to local high stress, then propagates along the horizontal interface towards the right edge of the specimen, ultimately resulting in the structural failure. Figure C.12 (b) compares the displacement results at the moment when crack fully propagates (see Figure C.12 (c)), which are obtained by the CPF model and the CZM, respectively. A distinct displacement jump is observable in the CZM at the interface, while the displacement field in the phase-field simulation maintains continuity with a smooth transition at the crack site. Despite these differences, both models yield consistent predictions regarding the global displacement profile. Besides, interface Model-S2 and Model-E2 give consistent predictions on fracture evolution path, despite different (stair-wise of exponential) representations of interface adopted in the simulations.

What draws more attentions are quantitative structural reaction forces in Figure C.12 (d) and (e). Numerically predicted loads F^{*} versus displacements u^{*} under varying b and L are compared. The results produced by the CPF model, reveal consistent trends with an initially linear elastic regime followed by a sudden drop attributed to the com-

plete propagation of brittle cracks. Nevertheless, interface Model-S0, Model-S1, Model-E0 and Model-E1 exhibit inconsistent peak structure bearing capacities with predictions from the cohesive zone model, demonstrating significant dependencies on length-scale parameters b and L. This can be attributed to the imprecise evaluation of interface fracture energy, as listed in Table 1. With introduced effective interface fracture energy in the CPF framework to realize the equivalence to the sharp interface fracture energy, length-scale insensitive results consistent with CZM predictions can be attained, irrespective of whether stair-wise (Model-S2) or exponential (Model-E2) representation of interface fracture energy is employed.

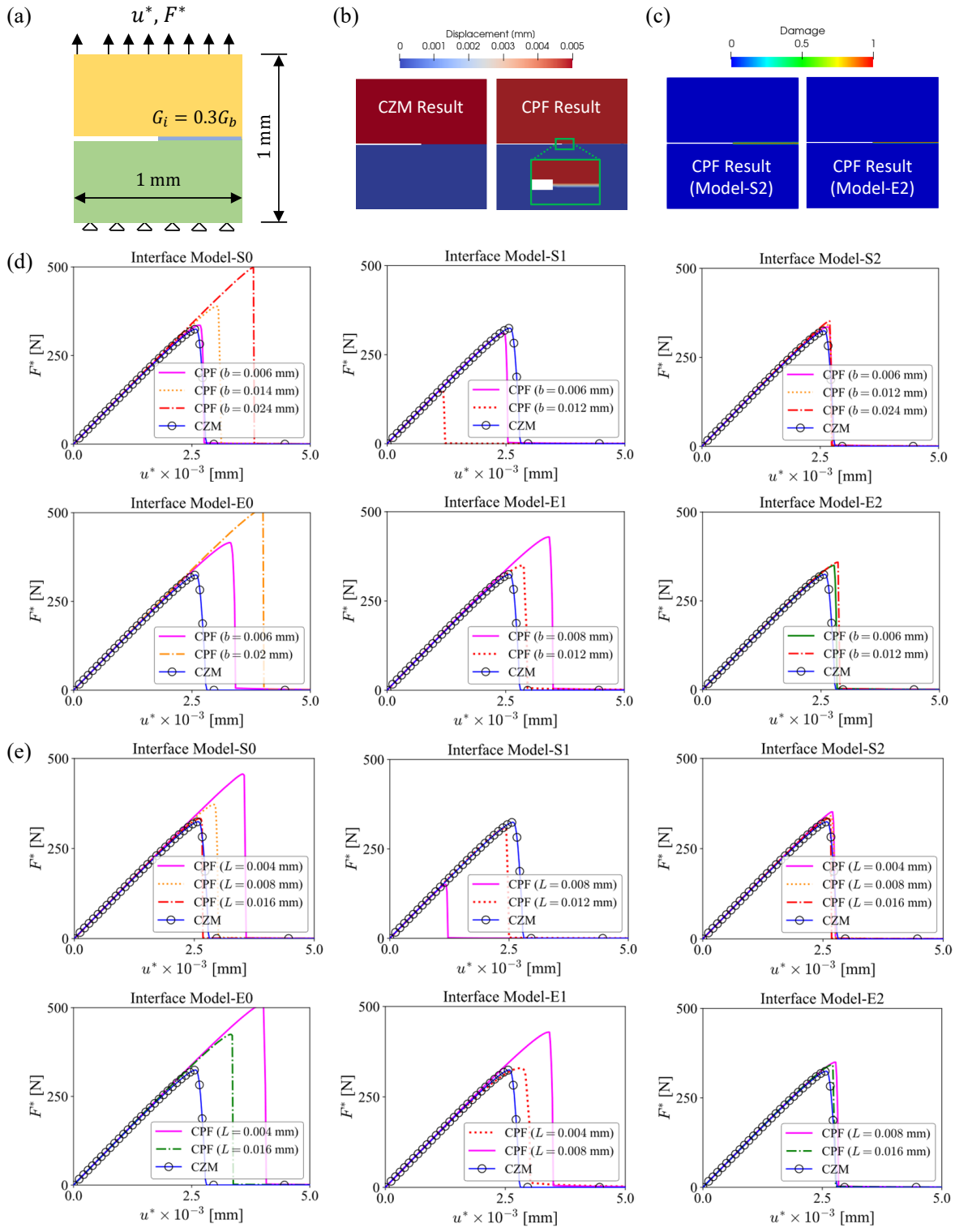

Figure C.12: Single-edge notched plate with a horizontal interface under vertical mechanical loading. Figure (a) schematically illustrates the geometry with predefined notch and interface, and also the boundary conditions. Figure (b) compares the displacement results obtained by the CZM and the CPF model. Figure (c) compares the crack results obtained by phase-field interface fracture Model-S2 and Model-E2. Figure (d) compares structural reaction forces predicted by the CPF model and CZM in order to study the influence of b; for all simulations conducted with CPF, identical value $L = 0.008$ mm is adopted. Figure (e) compares structural reaction forces predicted by the CPF model and CZM for studying the influence of L, identical value $b = 0.012$ mm is adopted for all simulations conducted with CPF.

References

[1] G. Li, J. Yuan, Y. Zhang, N. Zhang, K. Liew, Microstructure and mechanical performance of graphene reinforced cementitious composites, Composites Part A: Applied Science and Manufacturing 114 (2018) 188–195. 1

[2] N. P. Padture, M. Gell, E. H. Jordan, Thermal barrier coatings for gas-turbine engine applications, Science 296 (5566) (2002) 280–284. 1

[3] J.-Y. Ye, L.-W. Zhang, Damage evolution of polymer-matrix multiphase composites under coupled moisture effects, Computer Methods in Applied Mechanics and Engineering 388 (2022) 114213. 1

[4] R. Khan, Fiber bridging in composite laminates: A literature review, Composite Structures 229 (2019) 111418. 1

[5] C. Sandino, P. Kroliczek, D. D. McErlain, S. K. Boyd, Predicting the permeability of trabecular bone by micro-computed tomography and finite element modeling, Journal of biomechanics 47 (12) (2014) 3129–3134. 1

[6] H.-H. Ryu, K.-J. Park, C. S. Yoon, Y.-K. Sun, Capacity fading of Ni-rich Li $[Ni_xCo_yMn_{1-x-y}]$ O_2 $(0.6 \leq x \leq 0.95)$ cathodes for high-energy-density lithium-ion batteries: Bulk or surface degradation?, Chemistry of materials 30 (3) (2018) 1155–1163. 1, 4

[7] H. Liu, M. Wolfman, K. Karki, Y.-S. Yu, E. A. Stach, J. Cabana, K. W. Chapman, P. J. Chupas, Intergranular cracking as a major cause of long-term capacity fading of layered cathodes, Nano letters 17 (6) (2017) 3452–3457. 2, 4, 5, 30

[8] A. Needleman, A continuum model for void nucleation by inclusion debonding, ASME. J. Appl. Mech. 54 (3) (1987) 525—531. 2

[9] X.-P. Xu, A. Needleman, Numerical simulations of fast crack growth in brittle solids, Journal of the Mechanics and Physics of Solids 42 (9) (1994) 1397–1434. 2

[10] M. Elices, G. Guinea, J. Gomez, J. Planas, The cohesive zone model: advantages, limitations and challenges, Eng. Fract. Mech. 69 (2) (2002) 137–163. 2, 4, 5, 26

[11] H. Amor, J.-J. Marigo, C. Maurini, Regularized formulation of the variational brittle fracture with unilateral contact: Numerical experiments, J. Mech. Phys. Solids 57 (8) (2009) 1209–1229. 2, 7, 17

[12] C. Miehe, F. Welschinger, M. Hofacker, Thermodynamically consistent phase-field models of fracture: Variational principles and multi-field FE implementations, Int. J. Numer. Methods Eng. 83 (10) (2010) 1273–1311. 2, 4, 7, 17

[13] J. Y. Wu, A unified phase-field theory for the mechanics of damage and quasi-brittle failure, J. Mech. Phys. Solids 103 (2017) 72–99. 2, 7, 15, 16, 19

[14] J. Y. Wu, V. P. Nguyen, A length scale insensitive phase-field damage model for brittle fracture, J. Mech. Phys. Solids 119 (2018) 20–42. 2, 3

[15] M. Paggi, J. Reinoso, Revisiting the problem of a crack impinging on an interface: A modeling framework for the interaction between the phase field approach for brittle fracture and the interface cohesive zone model, Computer Methods in Applied Mechanics and Engineering 321 (2017) 145–172. 2, 3, 19

[16] V. Carollo, J. Reinoso, M. Paggi, A 3D finite strain model for intralayer and interlayer crack simulation coupling the phase field approach and cohesive zone model, Composite Structures 182 (2017) 636–651.

[17] M. Corrado, M. Paggi, J. Reinoso, Dynamic formulation of phase field fracture in heterogeneous media with finite thickness cohesive interfaces, Computational Materials Science 205 (2022) 111226. 2, 3

[18] T.-T. Nguyen, J. Yvonnet, Q.-Z. Zhu, M. Bornert, C. Chateau, A phase-field method for computational modeling of interfacial damage interacting with crack propagation in realistic microstructures obtained by microtomography, Computer Methods in Applied Mechanics and Engineering 312 (2016) 567–595. 3, 5, 8, 10, 12

[19] T.-T. Nguyen, J. Réthoré, J. Yvonnet, M.-C. Baietto, Multi-phase-field modeling of anisotropic crack propagation for polycrystalline materials, Computational Mechanics 60 (2017) 289–314. 3, 16, 30, 33

[20] P. Zhang, W. Yao, X. Hu, T. Q. Bui, 3D micromechanical progressive failure simulation for fiber-reinforced composites, Composite Structures 249 (2020) 112534. 8, 10, 12

[21] G. Li, B. Yin, L. Zhang, K. Liew, Modeling microfracture evolution in heterogeneous composites: A coupled cohesive phase-field model, Journal of the Mechanics and Physics of Solids 142 (2020) 103968. 3, 8, 10

[22] G. Li, B. Yin, L. Zhang, K. Liew, A framework for phase-field modeling of interfacial debonding and frictional slipping in heterogeneous composites, Computer Methods in Applied Mechanics and Engineering 382 (2021) 113872. 3, 8, 10

[23] T.-T. Nguyen, D. Waldmann, T. Q. Bui, Role of interfacial transition zone in phase field modeling of fracture in layered heterogeneous structures, Journal of Computational Physics 386 (2019) 585–610. 3

[24] A. Singh, S. Pal, Chemo-mechanical modeling of inter-and intra-granular fracture in heterogeneous cathode with polycrystalline particles for lithium-ion battery, J. Mech. Phys. Solids 163 (2022) 104839. 3, 5, 16, 21, 29, 30

[25] H. C. Parks, A. M. Boyce, A. Wade, T. M. Heenan, C. Tan, E. Martínez-Pañeda, P. R. Shearing, D. J. Brett, R. Jervis, Direct observations of electrochemically induced intergranular cracking in polycrystalline NMC811 particles, Journal of Materials Chemistry A 11 (39) (2023) 21322–21332. 30

[26] A. Singh, J. Song, W. Li, T. Martin, H. Xu, D. P. Finegan, J. Zhu, Microstructure-chemomechanics relations of polycrystalline cathodes in solid-state batteries, Extreme Mechanics Letters (2024) 102164. 3, 5

[27] A. C. Hansen-Dörr, R. de Borst, P. Hennig, M. Kästner, Phase-field modelling of interface failure in brittle materials, Comput. Methods Appl. Mech. Eng. 346 (2019) 25–42. 3, 8, 10, 19, 34

[28] A. C. Hansen-Dörr, F. Dammaß, R. de Borst, M. Kästner, Phase-field modeling of crack branching and deflection in heterogeneous media, Engineering Fracture Mechanics 232 (2020) 107004. 3, 8, 10, 34

[29] K. Yoshioka, M. Mollaali, O. Kolditz, Variational phase-field fracture modeling with interfaces, Computer Methods in Applied Mechanics and Engineering 384 (2021) 113951. 3, 8, 10, 34, 35

[30] Q. Zhou, L. Yang, C. Luo, F. Chen, Y. Zhou, Y. Wei, Thermal barrier coatings failure mechanism during the interfacial oxidation process under the interaction between interface by cohesive zone model and brittle fracture by phase-field, International Journal of Solids and Structures 214 (2021) 18–34. 3

[31] W.-X. Chen, J. M. Allen, S. Rezaei, O. Furat, V. Schmidt, A. Singh, P. J. Weddle, K. Smith, B.-X. Xu, Cohesive phase-field chemo-mechanical simulations of inter-and trans-granular fractures in polycrystalline NMC cathodes via image-based 3D reconstruction, Journal of Power Sources 596 (2024) 234054. 3, 4, 5, 8, 10, 18, 28, 29, 30, 34

[32] J. Schnell, T. Günther, T. Knoche, C. Vieider, L. Köhler, A. Just, M. Keller, S. Passerini, G. Reinhart, All-solid-state lithium-ion and lithium metal batteries–paving the way to large-scale production, Journal of Power Sources 382 (2018) 160–175. 3

[33] P. Albertus, V. Anandan, C. Ban, N. Balsara, I. Belharouak, J. Buettner-Garrett, Z. Chen, C. Daniel, M. Doeff, N. J. Dudney, et al., Challenges for and pathways toward Li-metal-based all-solid-state batteries (2021). 3

[34] Y. Zhao, P. Stein, Y. Bai, M. Al-Siraj, Y. Yang, B.-X. Xu, A review on modeling of electro-chemo-mechanics in lithium-ion batteries, Journal of Power Sources 413 (2019) 259–283. 4

[35] X. Gao, Y.-N. Zhou, D. Han, J. Zhou, D. Zhou, W. Tang, J. B. Goodenough, Thermodynamic understanding of Li-dendrite formation, Joule 4 (9) (2020) 1864–1879. 4

[36] M. T. McDowell, I. Ryu, S. W. Lee, C. Wang, W. D. Nix, Y. Cui, Studying the kinetics of crystalline silicon nanoparticle lithiation with in situ transmission electron microscopy, Advanced Materials 24 (45) (2012) 6034–6041. 4

[37] R. Xu, H. Sun, L. S. de Vasconcelos, K. Zhao, Mechanical and structural degradation of $LiNi_xMn_yCo_zO_2$ cathode in Li-ion batteries: An experimental study, Journal of The Electrochemical Society 164 (13) (2017) A3333. 4

[38] E. J. Cheng, A. Sharafi, J. Sakamoto, Intergranular Li metal propagation through polycrystalline $Li_{6.25}Al_{0.25}La_3Zr_2O_{12}$ ceramic electrolyte, Electrochimica Acta 223 (2017) 85–91. 4

[39] R. Koerver, I. Aygün, T. Leichtweiß, C. Dietrich, W. Zhang, J. O. Binder, P. Hartmann, W. G. Zeier, J. Janek, Capacity fade in solid-state batteries: Interphase formation and chemomechanical processes in nickel-rich layered oxide cathodes and lithium thiophosphate solid electrolytes, Chemistry of Materials 29 (13) (2017) 5574–5582. 4

[40] O. Furat, D. P. Finegan, D. Diercks, F. Usseglio-Viretta, K. Smith, V. Schmidt, Mapping the architecture of single lithium ion electrode particles in 3D, using electron backscatter diffraction and machine learning segmentation, Journal of Power Sources 483 (2021) 229148. 4

[41] A. Quinn, H. Moutinho, F. Usseglio-Viretta, A. Verma, K. Smith, M. Keyser, D. P. Finegan, Electron backscatter diffraction for investigating

lithium-ion electrode particle architectures, Cell Reports Physical Science 1 (8) (2020). 4

[42] B. Song, S. J. Day, T. Sui, L. Lu, C. C. Tang, A. M. Korsunsky, Mitigated phase transition during first cycle of a Li-rich layered cathode studied by in operando synchrotron X-ray powder diffraction, Physical Chemistry Chemical Physics 18 (6) (2016) 4745–4752. 4

[43] K. Nakajima, F. L. Souza, A. L. Freitas, A. Thron, R. H. Castro, Improving thermodynamic stability of nano-$LiMn_2O_4$ for Li-ion battery cathode, Chemistry of Materials 33 (11) (2021) 3915–3925. 4, 5, 30

[44] H. Kim, M. G. Kim, H. Y. Jeong, H. Nam, J. Cho, A new coating method for alleviating surface degradation of $LiNi_{0.6}Co_{0.2}Mn_{0.2}O_2$ cathode material: nanoscale surface treatment of primary particles, Nano Lett. 15 (3) (2015) 2111–2119. 4, 5

[45] F. Lin, I. M. Markus, D. Nordlund, T.-C. Weng, M. D. Asta, H. L. Xin, M. M. Doeff, Surface reconstruction and chemical evolution of stoichiometric layered cathode materials for lithium-ion batteries, Nat. Commun. 5 (1) (2014) 3529. 4

[46] P. Yan, J. Zheng, M. Gu, J. Xiao, J.-G. Zhang, C.-M. Wang, Intragranular cracking as a critical barrier for high-voltage usage of layer-structured cathode for lithium-ion batteries, Nat. Commun. 8 (1) (2017) 14101. 4, 5, 30

[47] G. Qian, Y. Zhang, L. Li, R. Zhang, J. Xu, Z. Cheng, S. Xie, H. Wang, Q. Rao, Y. He, et al., Single-crystal nickel-rich layered-oxide battery cathode materials: synthesis, electrochemistry, and intra-granular fracture, Energy Storage Mater. 27 (2020) 140–149. 4, 5, 30

[48] M. Klinsmann, D. Rosato, M. Kamlah, R. M. McMeeking, Modeling crack growth during Li extraction in storage particles using a fracture phase field approach, J. Electrochem. Soc. 163 (2) (2015) A102. 4, 5, 30

[49] H.-K. Tian, A. Chakraborty, A. A. Talin, P. Eisenlohr, Y. Qi, Evaluation of the electrochemo-mechanically induced stress in all-solid-state Li-ion batteries, Journal of The Electrochemical Society 167 (9) (2020) 090541. 4

[50] P. Stein, B. Xu, 3D isogeometric analysis of intercalation-induced stresses in Li-ion battery electrode particles, Comput. Methods Appl. Mech. Eng. 268 (2014) 225–244.

[51] C. V. Di Leo, E. Rejovitzky, L. Anand, A Cahn–Hilliard-type phase-field theory for species diffusion coupled with large elastic deformations: Application to phase-separating Li-ion electrode materials, J. Mech. Phys. Solids 70 (2014) 1–29. 4

[52] Y. Zhao, P. Stein, B.-X. Xu, Isogeometric analysis of mechanically coupled Cahn–Hilliard phase segregation in hyperelastic electrodes of Li-ion batteries, Comput. Methods Appl. Mech. Eng. 297 (2015) 325–347. 4

[53] G. Bucci, T. Swamy, Y.-M. Chiang, W. C. Carter, Modeling of internal mechanical failure of all-solid-state batteries during electrochemical cycling, and implications for battery design, Journal of Materials Chemistry A 5 (36) (2017) 19422–19430. 4

[54] W. Ai, B. Wu, E. Martínez-Pañeda, A coupled phase field formulation for modelling fatigue cracking in lithium-ion battery electrode particles, J. Power Sources 544 (2022) 231805. 5, 17

[55] K. Taghikhani, P. J. Weddle, R. M. Hoffman, J. Berger, R. J. Kee, Electro-chemo-mechanical finite-element model of single-crystal and polycrystalline NMC cathode particles embedded in an argyrodite solid electrolyte, Electrochim. Acta 460 (2023) 142585. 4, 29

[56] A. Singh, S. Pal, Coupled chemo-mechanical modeling of fracture in polycrystalline cathode for lithium-ion battery, International Journal of Plasticity 127 (2020) 102636. 4, 30

[57] Y. Bai, K. Zhao, Y. Liu, P. Stein, B.-X. Xu, A chemo-mechanical grain boundary model and its application to understand the damage of Li-ion battery materials, Scripta Materialia 183 (2020) 45–49.

[58] S. Rezaei, A. Asheri, B.-X. Xu, A consistent framework for chemo-mechanical cohesive fracture and its application in solid-state batteries, J. Mech. Phys. Solids 157 (2021) 104612. 4, 21, 29, 36

[59] D. Bistri, A. Afshar, C. V. Di Leo, Modeling the chemo-mechanical behavior of all-solid-state batteries: a review., Meccanica 56 (2021) 1523–1554. 4

[60] V. S. Deshpande, R. M. McMeeking, Models for the interplay of mechanics, electrochemistry, thermodynamics, and kinetics in lithium-ion batteries, Applied Mechanics Reviews 75 (1) (2023) 010801. 4

[61] G. Sun, T. Sui, B. Song, H. Zheng, L. Lu, A. M. Korsunsky, On the fragmentation of active material secondary particles in lithium ion battery cathodes induced by charge cycling, Extreme Mech. Lett. 9 (2016) 449–458. 4

[62] R. Xu, K. Zhao, Corrosive fracture of electrodes in Li-ion batteries, J. Mech. Phys. Solids 121 (2018) 258–280. 21

[63] Y. Zhang, C. Zhao, Z. Guo, Simulation of crack behavior of secondary particles in Li-ion battery electrodes during lithiation/de-lithiation

cycles, Int. J. Mech. Sci. 155 (2019) 178–186.

[64] Y. Bai, D. A. Santos, S. Rezaei, P. Stein, S. Banerjee, B.-X. Xu, A chemo-mechanical damage model at large deformation: numerical and experimental studies on polycrystalline energy materials, Int. J. Solids Struct. 228 (2021) 111099. 4, 21, 36

[65] B. Bourdin, G. Francfort, J.-J. Marigo, The variational approach to fracture, Springer, Berlin, 2008. 4

[66] P. Zuo, Y.-P. Zhao, A phase field model coupling lithium diffusion and stress evolution with crack propagation and application in lithium ion batteries, Phys. Chem. Chem. Phys. 17 (1) (2015) 287–297. 5

[67] B.-X. Xu, Y. Zhao, P. Stein, Phase field modeling of electrochemically induced fracture in Li-ion battery with large deformation and phase segregation, GAMM-Mitteilungen 39 (1) (2016) 92–109.

[68] Y. Zhao, B.-X. Xu, P. Stein, D. Gross, Phase-field study of electrochemical reactions at exterior and interior interfaces in Li-ion battery electrode particles, Comput. Methods Appl. Mech. Eng. 312 (2016) 428–446. 15, 29

[69] C. Miehe, H. Dal, L.-M. Schänzel, A. Raina, A phase-field model for chemo-mechanical induced fracture in lithium-ion battery electrode particles, Int. J. Numer. Methods Eng. 106 (9) (2016) 683–711.

[70] A. Mesgarnejad, A. Karma, Phase field modeling of chemomechanical fracture of intercalation electrodes: Role of charging rate and dimensionality, J. Mech. Phys. Solids 132 (2019) 103696. 30

[71] A. M. Boyce, E. Martínez-Pañeda, A. Wade, Y. S. Zhang, J. J. Bailey, T. M. Heenan, D. J. Brett, P. R. Shearing, Cracking predictions of lithium-ion battery electrodes by X-ray computed tomography and modelling, J. Power Sources 526 (2022) 231119.

[72] X. Cao, Y. Lu, Z. Chen, K. Zhang, F. Wang, A chemo-mechanical phase-field framework for dynamic fracture with viscoplastic flow for large-deformed electrode in lithium-ion batteries, Journal of Alloys and Compounds 965 (2023) 171387.

[73] T. Zhang, M. Kamlah, R. M. McMeeking, Modeling storage particle delamination and electrolyte cracking in cathodes of solid state batteries, Journal of the Mechanics and Physics of Solids 185 (2024) 105551. 5

[74] S. Rezaei, J. N. Okoe-Amon, C. A. Varkey, A. Asheri, H. Ruan, B.-X. Xu, A cohesive phase-field fracture model for chemo-mechanical environments: Studies on degradation in battery materials, Theor. Appl. Fract. Mech. 124 (2023) 103758. 5, 8, 10, 15, 17, 34

[75] A. Gustafsson, H. Isaksson, Phase field models of interface failure for bone application-evaluation of open-source implementations, Theor. Appl. Fract. Mech. 121 (2022) 103432. 8, 10, 34

[76] Q. Zhou, Y. Wei, Y. Zhou, L. Yang, An interface-width-insensitive cohesive phase-field model for fracture evolution in heterogeneous materials, International Journal of Solids and Structures 256 (2022) 111980. 8, 10, 34, 35

[77] J. Carlsson, P. Isaksson, Simulating fracture in a wood microstructure using a high-resolution dynamic phase field model, Engineering Fracture Mechanics 232 (2020) 107030. 10

[78] F. Vicentini, P. Carrara, L. De Lorenzis, Phase-field modeling of brittle fracture in heterogeneous bars, European Journal of Mechanics-A/Solids 97 (2023) 104826. 11

[79] P. Zhang, X. Hu, S. Yang, W. Yao, Modelling progressive failure in multi-phase materials using a phase field method, Engineering Fracture Mechanics 209 (2019) 105–124. 12

[80] W.-X. Chen, J.-Y. Wu, Phase-field cohesive zone modeling of multi-physical fracture in solids and the open-source implementation in Comsol Multiphysics, Theor. Appl. Fract. Mech. 117 (2022) 103153. 16, 18

[81] J. M. Allen, P. J. Weddle, A. Verma, A. Mallarapu, F. Usseglio-Viretta, D. P. Finegan, A. M. Colclasure, W. Mai, V. Schmidt, O. Furat, et al., Quantifying the influence of charge rate and cathode-particle architectures on degradation of Li-ion cells through 3D continuum-level damage models, J. Power Sources 512 (2021) 230415. 16, 17, 21, 28, 29

[82] M. E. Ferraro, B. L. Trembacki, V. E. Brunini, D. R. Noble, S. A. Roberts, Electrode mesoscale as a collection of particles: coupled electrochemical and mechanical analysis of nmc cathodes, Journal of The Electrochemical Society 167 (1) (2020) 013543. 16

[83] K. Taghikhani, P. J. Weddle, R. M. Hoffman, J. Berger, R. J. Kee, Electro-chemo-mechanical finite-element model of single-crystal and polycrystalline nmc cathode particles embedded in an argyrodite solid electrolyte, Electrochimica Acta 460 (2023) 142585. 16, 29

[84] A. Valverde-González, E. Martínez-Pañeda, A. Quintanas-Corominas, J. Reinoso, M. Paggi, Computational modelling of hydrogen assisted fracture in polycrystalline materials, International Journal of Hydrogen Energy 47 (75) (2022) 32235–32251.

[85] M. Paggi, M. Corrado, J. Reinoso, Fracture of solar-grade anisotropic polycrystalline silicon: A combined phase field–cohesive zone model approach, Computer Methods in Applied Mechanics and Engineering 330 (2018) 123–148. 16, 30, 33

[86] B. D. Coleman, M. E. Gurtin, Thermodynamics with internal state variables, Int. J. Chem. Phys. 47 (2) (1967) 597–613. 16

[87] N. P. van Dijk, J. J. Espadas-Escalante, P. Isaksson, Strain energy density decompositions in phase-field fracture theories for orthotropy and anisotropy, Int. J. Solids Struct. 196 (2020) 140–153. 17

[88] V. Ziaei-Rad, M. Mollaali, T. Nagel, O. Kolditz, K. Yoshioka, Orthogonal decomposition of anisotropic constitutive models for the phase field approach to fracture, J. Mech. Phys. Solids 171 (2023) 105143. 17

[89] J.-Y. Wu, V. P. Nguyen, H. Zhou, Y. Huang, A variationally consistent phase-field anisotropic damage model for fracture, Comput. Methods Appl. Mech. Eng. 358 (2020) 112629. 17

[90] J.-Y. Wu, W.-X. Chen, Phase-field modeling of electromechanical fracture in piezoelectric solids: Analytical results and numerical simulations, Computer Methods in Applied Mechanics and Engineering 387 (2021) 114125. 17

[91] H. Ming-Yuan, J. W. Hutchinson, Crack deflection at an interface between dissimilar elastic materials, International Journal of Solids and Structures 25 (9) (1989) 1053–1067. 19, 21, 22, 23, 26

[92] J. W. Hutchinson, Z. Suo, Mixed mode cracking in layered materials, Advances in Applied Mechanics 29 (1991) 63–191. 19, 21, 22, 23, 26

[93] O. Furat, J. Petrich, D. Finegan, D. Diercks, F. Usseglio-Viretta, K. Smith, V. Schmidt, Artificial generation of representative single Li-ion electrode particle architectures from microscopy data, npj Comput. Mater. 7 (2021) 105. 28

[94] A. P. Tran, S. Yan, Q. Fang, Improving model-based functional near-infrared spectroscopy analysis using mesh-based anatomical and light-transport models, Neurophotonics 7 (1) (2020) 015008–015008. 28

[95] S. Yamakawa, H. Yamasaki, T. Koyama, R. Asahi, Effect of microstructure on discharge properties of polycrystalline $LiCoO_2$, Solid State Ion. 262 (2014) 56–60. 29

[96] S. A. Roberts, V. E. Brunini, K. N. Long, A. M. Grillet, A framework for three-dimensional mesoscale modeling of anisotropic swelling and mechanical deformation in lithium-ion electrodes, J. Electrochem. Soc. 161 (11) (2014) F3052.

[97] J.-M. Lim, H. Kim, K. Cho, M. Cho, Fundamental mechanisms of fracture and its suppression in Ni-rich layered cathodes: Mechanics-based multiscale approaches, Extreme Mech. Lett. 22 (2018) 98–105. 29

[98] A. M. Colclasure, A. R. Dunlop, S. E. Trask, B. J. Polzin, A. N. Jansen, K. Smith, Requirements for enabling extreme fast charging of high energy density Li-ion cells while avoiding lithium plating, J. Electrochem. Soc. 166 (8) (2019) A1412. 29

[99] K. Min, C. Jung, D.-S. Ko, K. Kim, J. Jang, K. Park, E. Cho, High-performance and industrially feasible Ni-rich layered cathode materials by integrating coherent interphase, ACS applied materials & interfaces 10 (24) (2018) 20599–20610. 31

[100] X. Liu, B. Zheng, J. Zhao, W. Zhao, Z. Liang, Y. Su, C. Xie, K. Zhou, Y. Xiang, J. Zhu, et al., Electrochemo-mechanical effects on structural integrity of Ni-rich cathodes with different microstructures in all solid-state batteries, Advanced Energy Materials 11 (8) (2021) 2003583. 31

[101] M. Klinsmann, D. Rosato, M. Kamlah, R. M. McMeeking, Modeling crack growth during Li insertion in storage particles using a fracture phase field approach, Journal of the Mechanics and Physics of Solids 92 (2016) 313–344. 30

[102] M. Klinsmann, D. Rosato, M. Kamlah, R. M. McMeeking, Modeling crack growth during Li extraction and insertion within the second half cycle, Journal of power sources 331 (2016) 32–42. 30

[103] T. R. Tanim, P. J. Weddle, Z. Yang, A. M. Colclasure, H. Charalambous, D. P. Finegan, Y. Lu, M. Preefer, S. Kim, J. M. Allen, et al., Enabling extreme fast-charging: Challenges at the cathode and mitigation strategies, Adv. Energy Mater. 12 (46) (2022) 2202795. 33

[104] R. Ruess, S. Schweidler, H. Hemmelmann, G. Conforto, A. Bielefeld, D. A. Weber, J. Sann, M. T. Elm, J. Janek, Influence of NCM particle cracking on kinetics of lithium-ion batteries with liquid or solid electrolyte, J. Electrochem. Soc. 167 (10) (2020) 100532. 33

[105] P. Stein, Y. Zhao, B.-X. Xu, Effects of surface tension and electrochemical reactions in Li-ion battery electrode nanoparticles, Journal of Power Sources 332 (2016) 154–169. 33

[106] P. Camanho, C. Dávila, Mixed-mode dechoesion finite elements for the simulation of delamination in composite materials, NASA/TM-2002-211737 1 (01 2002). 36